https://doi.org/10.5194/amt-2023-233
Preprint. Discussion started: 14 November 2023

Atmospheric Measurement Techniques
Discussions

Synthetic mapping of XCO_2 retrieval performance from shortwave infrared measurements: impact of spectral resolution, signal-to-noise ratio and spectral band selection

Matthieu Dogniaux[1],*, Cyril Crevoisier[1]

[1]Laboratoire de Météorologie Dynamique/IPSL, CNRS, École polytechnique, Institut Polytechnique de Paris, Sorbonne Université, École Normale Supérieure, PSL Research University, 91120 Palaiseau, France
*now at: SRON Netherlands Institute for Space Research, Leiden, The Netherlands

Correspondence to: Matthieu Dogniaux (M.Dogniaux@sron.nl)

Abstract. Satellites have been providing spaceborne observations of the total column of CO_2 (noted X_{CO_2}) for over two decades now and, with the need for independent verification of Paris Agreement objectives, many new satellite concepts are currently planned or being studied to complement or extend the already existing instruments. Depending on whether they are targeting natural and/or anthropogenic fluxes of CO_2, the design of these future concepts vary greatly. The characteristics of their shortwave infrared (SWIR) observations notably explore several orders of magnitude in spectral resolution (from $\lambda/\Delta\lambda$~400 for Carbon Mapper to $\lambda/\Delta\lambda$~25000 for MicroCarb) and include different selections of spectral bands (from one to four bands, among which the CO_2-sensitive 1.6 µm and/or 2.05 µm bands). Besides, the very nature of the spaceborne measurements is also explored: for instance, the NanoCarb imaging concept proposes to measure CO_2-sensitive truncated interferograms, instead of infrared spectra as other concepts, in order to significantly reduce the instrument size. This study synthetically explores the impact of three different design parameters on X_{CO_2} retrieval performance, as obtained through Optimal Estimation: (1) the spectral resolution; (2) the signal-to-noise ratio (SNR) and (3) the spectral band selection. Similar performance assessments are completed for the exactly-defined MicroCarb, Copernicus CO_2 Monitoring (CO_2M) and NanoCarb concepts. We show that improving SNR is more efficient than improving spectral resolution to increase X_{CO_2} precision when perturbating these parameters across two orders of magnitude, and that low-SNR and/or low spectral resolution yield X_{CO_2} with vertical sensitivities giving more weight to atmospheric layers close to the surface. The exploration of various spectral band combinations illustrates, especially for lower spectral resolutions, how including an O_2-sensitive band helps to increase optical path length information, and how the 2.05 µm CO_2-sensitive band contains more geophysical information than the 1.6 µm band. With very different characteristics, MicroCarb shows a CO_2 information content only slightly higher than CO_2M, which translates into lower X_{CO_2} random errors, by a factor ranging from 1.1 to 1.9 depending on the observational situation. The NanoCarb performance for a single pixel of its imager compares to concepts that measure spectra at low-SNR and low-spectral resolution but, as this novel concept would observe a given target several times during a single overpass, its performance improves when combining all the observations. Overall, the broad range of

https://doi.org/10.5194/amt-2023-233
Preprint. Discussion started: 14 November 2023

results obtained through this synthetic X_{CO_2} performance mapping hints at the future intercomparison challenges that the wide variety of upcoming CO_2-observing concepts will pose.

1 Introduction

Anthropogenic emissions of carbon dioxide (CO_2) are the main driver of climate of change (IPCC, 2021). The current understanding of the global carbon cycle compares results from bottom-up methods, that explicitly model CO_2-emitting and absorbing mechanisms, with those from top-down approaches, that rely on a set of CO_2 atmospheric concentration observations to find the CO_2 fluxes that best fit those observations (Friedlingstein et al., 2022). This last approach, called inverse atmospheric transport (e.g. Ciais et al., 2010), can ingest in-situ observations and/or space-borne remote estimations of CO_2 atmospheric concentration. The latter are produced through inverse radiative transfer that enables to find the atmospheric states (among which the CO_2 concentration) that best fit infrared satellite measurements made from space.

Shortwave infrared (SWIR) satellite measurements, which are sensitive – among others – to CO_2 concentration close to the surface, where fluxes take place, have now been exploited for two decades to retrieve the column-averaged dry-air mole fraction of CO_2 (also called 'total column' and noted X_{CO_2}). The pioneer ESA Scanning Imaging Absorption Spectrometer for Atmospheric Chartography (SCIAMACHY) instrument (Bovensmann et al., 1999) was the first to provide a global X_{CO_2} dataset. Its mission ended in 2012, and it was followed by the – still flying – JAXA/NIES Greenhouse gases Observing SATellites (GOSAT and GOSAT-2, e.g. Inoue et al., 2016; Noël et al., 2021; Taylor et al., 2022), NASA Orbiting Carbon Observatory-2 and -3 (OCO-2 and OCO-3, e.g. Taylor et al., 2023) and the Chinese TanSat (e.g. Yang et al., 2020). The global X_{CO_2} datasets produced by these missions have found applications for the study of natural carbon fluxes at global scale (e.g. Chevallier et al., 2019; Peiro et al., 2022) and also, even if it was not their primary ambition, for the monitoring of point-source anthropogenic emissions (e.g. Nassar et al., 2021; Reuter et al., 2019; Zheng et al., 2020).

These different missions will be followed by various concepts that are already planned or still being studied. First, the planned CNES MicroCarb mission (Bertaux et al., 2020; Pascal et al., 2017) is quite similar to OCO-2 regarding its observation strategy (spatial and spectral resolution, see Table 1, it includes an extra O_2-sensitive band) and mainly aims to provide information on natural CO_2 fluxes. The 2015 Paris Agreement and the five-year global stocktake system it set up have put in motion a global ambition for spaceborne monitoring of anthropogenic greenhouse gas emissions (mainly for CO_2 and methane, but the latter is not the focus of this work). Indeed, urban areas, that account for 0.5% of the ice-free continental surface (Liu et al., 2020; Lwasa et al., 2022), gather 70% fossil fuel-related emissions (Duren and Miller, 2012). For favourable meteorological conditions, CO_2 plumes arise from either hotspots, such as megacities, or point sources, such as coal-fired power plants (e.g. Kuhlmann et al., 2019). Those may then be observed with SWIR spaceborne imagers, depending on their precision and spatial resolution, and the emission rate associated with the imaged plume can then be

https://doi.org/10.5194/amt-2023-233
Preprint. Discussion started: 14 November 2023

inferred either with plume analysis/mass-balance approaches (e.g. Bovensmann et al., 2010; Varon et al., 2018) or within more usual inverse atmospheric schemes (e.g. Broquet et al., 2018; Pillai et al., 2016). Because an infrared detector has a limited number of pixels, future - planned or studied - CO_2 imaging concepts explore various trade-offs between spatial and spectral resolution, spectral band selection, and even compromise with the very nature of the measurements made by the instrument, when other constraints such as size and thus costs are taken into consideration. These concepts – not exclusively – include the European Copernicus CO_2 Monitoring (Meijer, 2020) mission, the Japanese Global Observing SATellite for Greenhouse gases and Water cycle (GOSAT-GW, Matsunaga and Tanimoto, 2022), the American non-profit Carbon Mapper initiative (https://carbonmapper.org/) based on the Next-Generation of NASA Airborne Visible/Infrared Imaging Spectrometer (AVIRIS-NG, Cusworth et al., 2021; Hamlin et al., 2011), the German CO2image concept (Strandgren et al., 2020; Wilzewski et al., 2020) or the European Space CARBon Observatory (SCARBO) H2020 concept, that does not measure spectra but only truncated interferograms (Brooker, 2018; Dogniaux et al., 2022; Gousset et al., 2019). Table 1 gathers the characteristics of upcoming or studied SWIR CO_2 observing satellite concepts, provided either in scientific articles (in this case citations are provided), in conference presentations (just the conference name and dates are given), or websites (just the hyperlink is given), as some of these concepts are quite recent.

Table 1. Measurement characteristics for some of the upcoming or studied SWIR CO_2 observing satellite concepts

Concept	Spatial resolution/swath	Spectral bands	Resolving power ($\lambda/\Delta\lambda$)	Reference
OCO-2	1.3x2.3 km^2/10 km	O_2: 0.76 µm CO_2: 1.6 µm CO_2: 2.05 µm	~18000 ~19800 ~19800	(Crisp et al., 2017)
MicroCarb	4.5x8.9 km^2/13.5 km	O_2: 0.76 µm CO_2: 1.6 µm CO_2: 2.05 µm O_2: 1.27 µm	~25400 ~25750 ~25800 ~25800	(Bertaux et al., 2020)
CO_2M	2x2 km^2/>250 km	O_2: 0.76 µm CO_2, CH_4: 1.6 µm CO_2: 2.05 µm	~6300 ~5400 ~5800	(Meijer, 2020)
GOSAT-GW	3x3 km^2/90 km and 10x10 km^2/920 km	O_2: 0.76 µm CO_2, CH_4: 1.6 µm	>14000 >8000	IWGGMS-17, 14th – 17th of June, 2021
CO2image	50x50 m^2/50 km	CO_2: 2.05 µm	~1600	(Strandgren et al., 2020)
Carbon Mapper	30x30 m^2/18 km	0.4 – 2.5 µm	~400 around 2.05 µm	https://carbonmapper.org/our-mission/technology/

SCARBO	2.3x2.3 km	km^2/195.5	Truncated interferograms sensitive to: O_2: 0.76 µm CO_2, CH_4: 1.6 µm CO_2: 2.05 µm	(Brooker, 2018; Dogniaux et al., 2022; Gousset et al., 2019)

The characteristics of an observing concept (nature of measurement, spectral resolution, spectral band selection, signal-to-noise ratio) translate into an X_{CO_2} retrieval performance that comprises (1) random error, (2) systematic error, and (3) vertical sensitivity. First, X_{CO_2} random error (or precision) impacts the a posteriori uncertainties of fluxes estimated in usual inverse atmospheric schemes (e.g. Rayner and O'Brien, 2001), and the detectability of CO_2 plumes for imaging concepts (e.g. Kuhlmann et al., 2019). In addition to random errors, systematic errors can hamper X_{CO_2} retrievals. Those can for example be due to forward radiative transfer modelling errors, like aerosol misknowledge (Houweling et al., 2005; Reuter et al., 2010), or a priori misknowledge of atmospheric state parameters (smoothing error, e.g. Connor et al., 2008). Spatially correlated systematic errors are especially detrimental in inverse atmospheric schemes (e.g. Broquet et al., 2018; Chevallier et al., 2007), whereas scene-wide systematic errors that do not correlate with the plume shape can cancel out when applying plume analysis techniques. Finally, the retrieved CO_2 total columns must be characterized by their vertical sensitivity, which illustrates to which atmospheric levels retrievals are sensitive (e.g. Boesch et al., 2011; Buchwitz et al., 2005).

The impact of SWIR measurement characteristics on X_{CO_2} retrieval performance have been partially examined in previous studies that relied on real measurements. For instance, Galli et al. (2014) assessed the performance of X_{CO_2} retrievals from GOSAT measurements which spectral resolution was degraded up to 6 times ($\lambda/\Delta\lambda \sim 3000 - 20000$), or Wu et al. (2020) performed a similar exercise with OCO-2 measurements degraded at CO_2M spectral resolution. Spectral band selection has also been studied: Wu et al. (2019) performed retrievals only using the 2.05 µm band of OCO-2 measurements and Wilzewski et al. (2020) considered single-band observations, from spectrally degraded 1.6 µm / 2.05 µm GOSAT band measurements ($\lambda/\Delta\lambda \sim 700 - 8100/6150$, respectively).

In this work, we perform a systematic survey that synthetically explores the impact of three parameters on X_{CO_2} retrieval performance, for the design of SWIR CO_2 observing satellite concepts: spectral resolution, signal-to-noise ratio (SNR) and spectral band selection. These choices are motivated by the characteristics gathered in Table 1. Indeed, two orders of magnitude in resolving power ($\lambda/\Delta\lambda$) separate Carbon Mapper (AVIRIS-NG) from MicroCarb. Exploring a wide range of SNR values on the top of different resolving powers will help to encompass all possible performance results from a wide variety of concepts that measure SWIR spectra. Finally, because CO2image is planned to only measure the 2.05 µm band, and GOSAT-GW the 0.76 µm and 1.6 µm bands, we will also study the impact of choosing different combinations of spectral bands. Synthetic calculations performed for a fictious concept with varying design parameters will help to map a

https://doi.org/10.5194/amt-2023-233
Preprint. Discussion started: 14 November 2023

large space of possible X_{CO_2} retrieval performances, to which those of the peculiar SCARBO concept will be compared, along with those of the upcoming MicroCarb and CO_2M missions.

This article is structured as follows: Section 2 describes the observing concepts considered in this work, and Section 3 details the materials and methods. Section 4 describes the results obtained for a fictious concept with varying design parameters and discusses them. It first focuses on the impact of spectral resolution and SNR, then on the impact of spectral resolution and spectral band selection, for which it also explores geophysical information entanglements. Finally, Section 5 discusses the performance results obtained for the exactly defined MicroCarb and CO_2M concepts, along with those of the peculiar NanoCarb concept, and how they compare to those of the fictious concept with varying design parameters. Section 6 highlights the conclusions of this work.

2 SWIR CO_2 observing satellite concepts

In this section, we provide the measurement characteristics that are used to model the different upcoming – real or fictitious – SWIR CO_2 observing satellite concepts. In order to reduce the number of dimensions to explore, we consider, for the purpose of this study, that the spectra-measuring concepts have an identical resolving power $\lambda/\Delta\lambda$ over all their spectral bands, as well as a constant spectral sampling ratio of 3 (which is the case for both MicroCarb and CO_2M, and is a design hypothesis for CO2image). All Instrument Spectral Response Functions (ISRFs) are treated as Gaussian functions with a Full Width at Half-Maximum (FWHM, $\Delta\lambda$) calculated from the resolving power $\lambda/\Delta\lambda$, with λ being the average spectral band wavelength.

2.1 MicroCarb and CO_2M

We consider two explicitly described upcoming concepts that will measure SWIR spectra: MicroCarb and the Copernicus CO_2 Monitoring (CO_2M) concept. The left panel of Fig. 1 illustrates their observations.

MicroCarb (Bertaux et al., 2020; Pascal et al., 2017) is the upcoming CNES CO_2 observing mission that will acquire SWIR spectra at high spectral resolution, thus following the steps of the currently flying OCO-2. Besides the increase in spectral resolution, its main novelty is the addition of the O_2 1.27 µm band that will provide additional optical path length information at wavelengths closer to those that contain CO_2 sensitivity, which may help to reduce aerosol-related errors. MicroCarb aims at retrieving X_{CO_2} with a precision below 1 ppm, and with the lowest possible systematic errors. In this work, we use the measurement characteristics presented in Table 2 to model the MicroCarb concept. In Sect. 5, where MicroCarb results are presented, the impact on performance of using both or just one of the O_2-sensitive will be discussed.

Table 2. MicroCarb measurement characteristics used in this work.

Spectral band	**1 (O_2 A-band)**	**2 (CO_2 weak band)**	**3 (CO_2 strong band)**	**4 (O_2 1.27 µm band)**
Wavelenghts (µm)	0.758 – 0.769	1.597 – 1.619	2.023 – 2.051	1.265 – 1.282
Resolving power ($\lambda/\Delta\lambda$)	25000	25000	25000	25000
Spectral sampling ratio	3	3	3	3
Reference radiance L_{ref} ($W/m^2cm^{-1}sr$)	4.38 x 10^{-3}	2.69 x 10^{-3}	9.95 x 10^{-4}	2.97 x 10^{-3}
Reference SNR SNR_{ref}	480	579	249	503

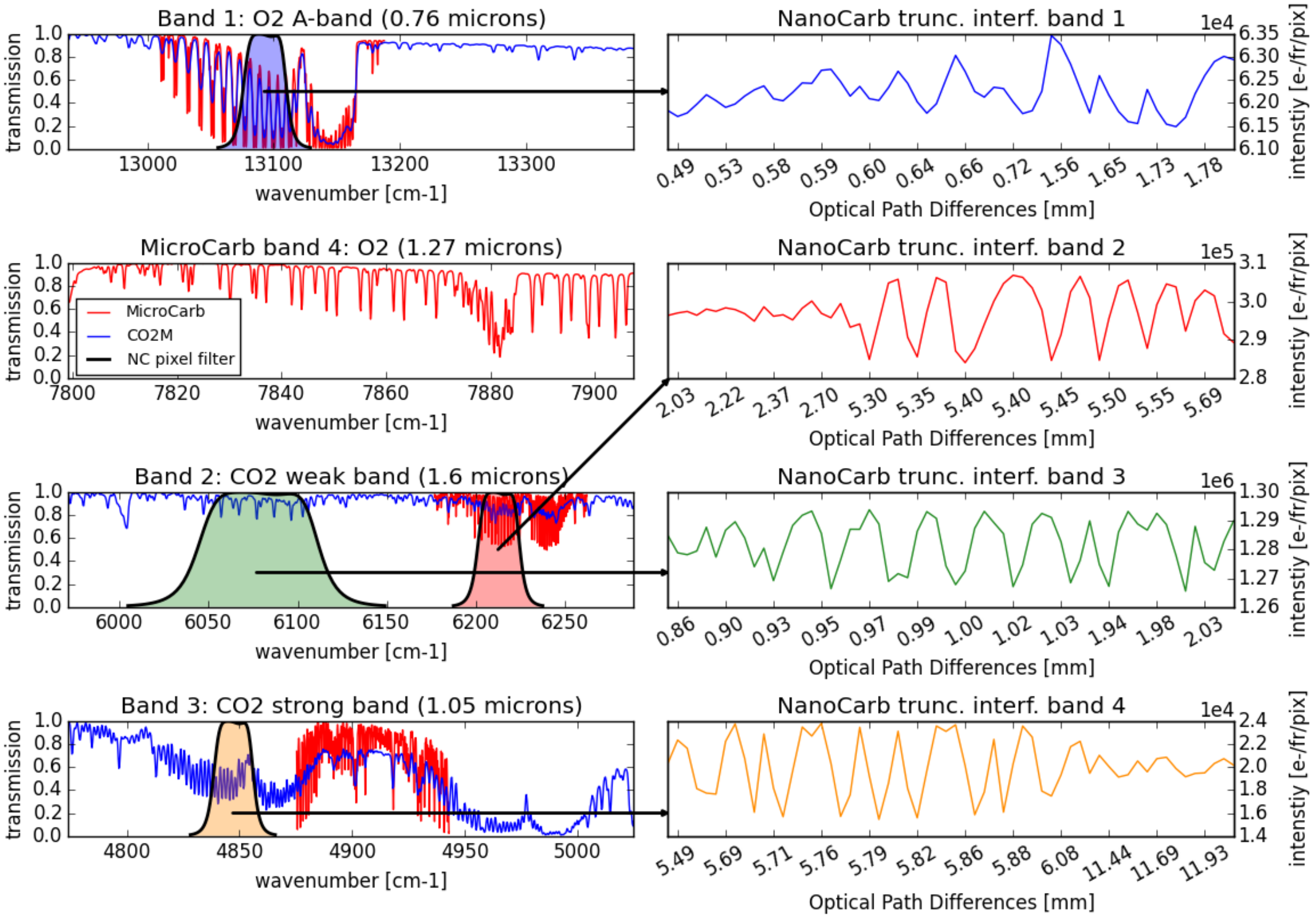

Figure 1. Example of CO_2M (blue) and MicroCarb (red) transmissions (left) and NanoCarb truncated interferogram (right) for a vegetation-like albedo with a Solar Zenith Angle of 50º. Arrows link NanoCarb bands to their respective narrow-band filters shown over CO_2M and MicroCarb transmissions.

The Copernicus CO_2 Monitoring (CO_2M) mission (Meijer, 2020) is the upcoming space component of the operational European anthropogenic CO_2 emissions Monitoring and Verification Support (CO_2MVS) capacity (Janssens-Maenhout et al., 2020). Its design compromises between spatial and spectral resolutions, swath and spectral band width, aiming to provide an imaging of X_{CO_2} with a random error lower than 0.7 ppm and systematic errors as low as possible. In this work, we use the measurement characteristics presented in Table 3 to model the CO_2M concept.

Table 3. CO_2M measurement characteristics used in this work.

Spectral band	**1 (O_2 A-band)**	**2 (CO_2 weak band)**	**3 (CO_2 strong band)**
Wavelenghts (µm)	0.747 – 0.773	1.590 – 1.675	1.990 – 2.095
Resolving power ($\lambda/\Delta\lambda$)	5870	5870	5870
Spectral sampling ratio	3	3	3
Reference radiance L_{ref} ($W/m^2cm^{-1}sr$)	9.66×10^{-4}	6.81×10^{-4}	7.30×10^{-4}
Reference SNR SNR_{ref}	330	400	400

2.2 Fictitiously Varying CO_2M concept (CVAR)

In order to grasp the full extent of upcoming or studied SWIR CO_2 observing satellite concepts, we also consider a fictitious concept that has the same characteristics as CO_2M, apart from its resolving power $\lambda/\Delta\lambda$, SNR and spectral band selection. This varying concept will be hereafter referred to as "CVAR".

First, we consider resolving power values ranging from 200 to 30000 (the list of exact resolving power values that are considered is given in the Supplements). Figure 2 illustrates the impact of spectral resolution on the CO_2 absorption band around 1.6 µm. For the lowest resolving power $\lambda/\Delta\lambda = 200$, the "two-lobed" P-R branch structure of this CO_2 absorption band (see e.g. Liou, 2002) is not visible. It fully appears from $\lambda/\Delta\lambda = 1000$ upwards. Individual absorption lines become visible, but are not fully resolved for $\lambda/\Delta\lambda$ comprised between about 1000 and 10000. Only for $\lambda/\Delta\lambda > 10000$ does the whole P-R band structure and individual absorption lines fully appear. Given that the fixed CO_2M spectral band intervals are quite large, compared to those of MicroCarb, the choice of using CO_2M band intervals for exploring the impact of the resolving power on X_{CO_2} retrieval performance is a reasonable compromise between high resolution instruments that measure narrow spectral bands (e.g MicroCarb or OCO-2), and low resolution instruments that measure a continuous spectra

https://doi.org/10.5194/amt-2023-233
Preprint. Discussion started: 14 November 2023

(e.g. Carbon Mapper from 0.4 to 2.5 µm). Thus, this compromise yields fictitiously large spectral bands for CVAR cases with high resolving power values, and corresponds to a window selection approach for observations with low spectral resolution, similar to what is actually done to process AVIRIS-NG measurements (Cusworth et al., 2021).

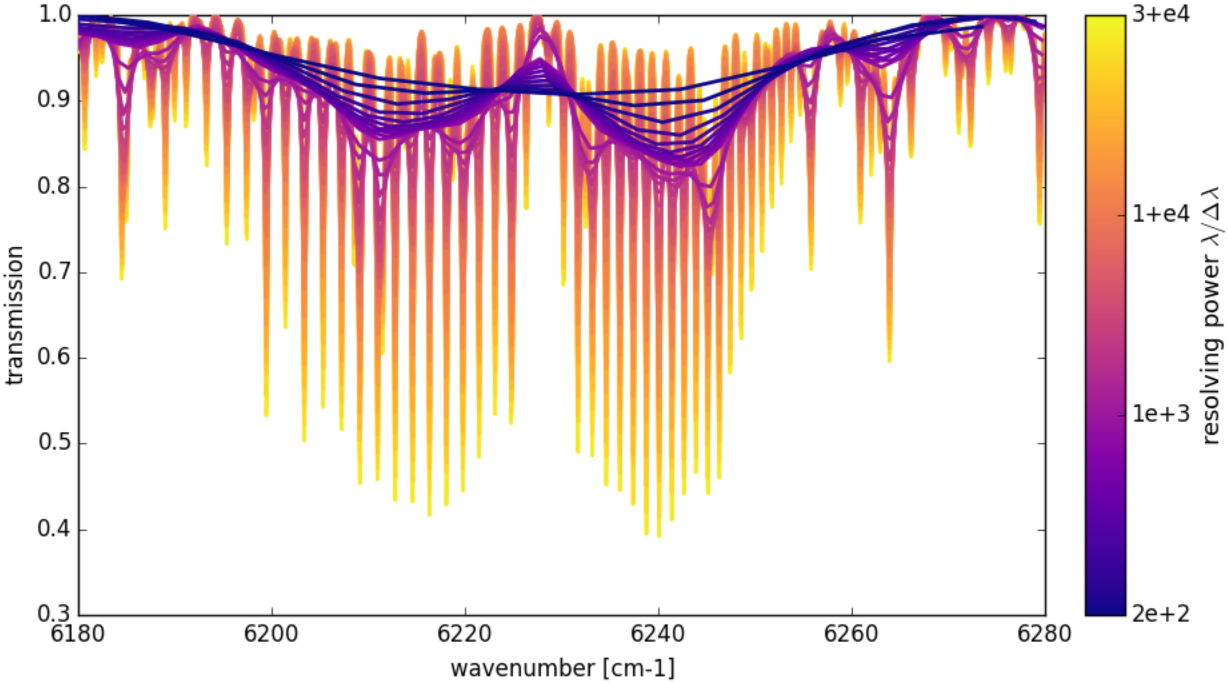

Figure 2. CO_2-sensitive 1.6 µm band observed with a resolving power $\lambda/\Delta\lambda$ ranging from 200 to 30000.

In addition to spectral resolution, we also consider the impact of SNR in this study. This will help to explore the performance of a wider range of SWIR CO_2 observing satellite concepts. We will cover two orders of magnitude in noise level by applying a spectral-band-wise factor ranging from 0.1 to 10 on CO_2M SNR values given in Table 3. The impacts of both spectral resolution and SNR on X_{CO_2} retrieval performance results are presented and discussed in Sect. 4.1.

Finally, in addition to spectral resolution but separately from SNR, we consider the impact of spectral band selection. This will help to encompass upcoming or studied single- or dual-band observing concepts such as CO2image or GOSAT-GW, respectively. All CO_2M spectral band combinations containing at least one CO_2-sensitive band will be explored: B2, B12, B3, B13, B23 and B123 (with B denoting "band" followed by the CO_2M spectral band numbers considered in the combination). The impacts of both spectral resolution and spectral band selection on X_{CO_2} retrieval performance results and geophysical information entanglement are presented and discussed in Sect. 4.2 and 4.3.

2.3 The SCARBO concept and NanoCarb

The Space CARBon Observatory (SCARBO) concept (Brooker, 2018) is quite different from all the other concepts mentioned in this article. Indeed, it relies on a miniaturized static Fabry-Perot interferometer, named NanoCarb, that measures truncated interferograms at Optical Path Differences (OPDs) which are optimally sensitive to CO_2, and to some other interfering geophysical variables (Gousset et al., 2019). Because of their very nature, these truncated interferograms are sensitive to the periodic signature of CO_2 in the infrared spectrum. As in Dogniaux et al. (2022), we use here the latest design of the NanoCarb instrument, which accounts for CO_2 information entanglements with H_2O and aerosols, while atmospheric temperature or albedo have been neglected. It measures truncated interferograms that are sensitive to four spectral bands, as shown in Fig. 1 right panel, which are associated to narrow-band filters shown in Fig. 1 left panel (follow the arrows). NanoCarb has a two-dimensional field-of-view (FOV, 170 across-track x 102 along-track pixels, in the current design) that observes a fixed location on the ground with different viewing angles, as it flies over it. The up to 102 X_{CO_2} retrievals that can be done for a same location on the ground are then combined to yield only one unique retrieval result, with reduced random error (assuming independent observations). Dogniaux et al. (2022) details the NanoCarb concept performance results and its current shortcomings. One of the main results is that NanoCarb performance decreases close to the FOV edges, so we will only focus here on the central FOV pixel, and central along-track row of pixels. Besides, it also explains that CO_2 and interfering geophysical variable information contents are entangled in NanoCarb truncated interferograms. This specific shortcoming will be further detailed in this article.

3 Materials and methods

3.1 Atmospheric and observational situations

We consider 12 atmospheric and observational situations that explore three surface albedo models (soil, vegetation and desert, denoted SOL, VEG and DES, respectively – their average values over the SWIR spectral bands are given in the Supplementary Table S2), generated from the ASTER spectral library (Baldridge et al., 2009), and 4 Solar Zenith Angles (hereafter SZA, 0°, 25°, 50° and 70°). A given situation will be referred to with its albedo model short name followed by the SZA, e.g. VEG-50º, for the situation with an albedo representative of vegetation, lit with an SZA equal to 50º.

For these 12 situations, the measurements are made at nadir (viewing zenith angle equal to 0°). We use a typically European atmospheric situation (vertical temperature and water vapour profiles), taken as the average of the mid-latitude temperate atmospheric profiles included in the Thermodynamic Initial Guess Retrieval (TIGR) climatology library (Chedin et al., 1985; Chevallier et al., 1998). For this synthetic performance study, we consider a constant vertical CO_2 concentration profile of 394.95 ppm. The surface pressure is constant and set at 1013 hPa. Fine-mode aerosols, representative of soot, are included between 0 and 2 km of altitude, and coarse mode aerosols, representative of minerals, are included between 2 and 4 km of altitude.

3.2 Performance evaluation with Optimal Estimation

3.2.1 General aspects

Optimal Estimation (hereafter OE, Rodgers, 2000) offers an ideal framework for the evaluation of X_{CO_2} retrieval performance. It has been extensively described in other publications (e.g. Connor et al., 2008), so only its essential aspects are reminded in this article. Given a state vector x that contains parameters that describe the atmospheric and surface state, and a measurement vector y that contains the infrared observation made from space by a studied concept, OE enables to provide the geophysical state that best fits the measurement made from space, thus giving a satisfying solution to the following equation:

$$y = F(x) + \varepsilon \quad (1)$$

with F, the forward radiative transfer model that allows to simulate spaceborne infrared observations from geophysical state parameters, and ε, the spaceborne measurement uncertainty. Because this inverse problem is ill-posed, OE brings in a priori information that helps to better constrain the estimation. This a priori information can be seen as the knowledge of the geophysical state one would have before using the information contained in the spaceborne measurement (e.g. taken from climatologies). It is given in the form of an a priori state vector x_a, characterized by its uncertainty given in the a priori state covariance matrix S_a.

The retrieved geophysical state that best fits the measurement made from space and the a priori information is called the maximum-likelihood a posteriori state and is noted $\hat{x}$. Its a posteriori covariance matrix, which describes the uncertainty of the retrieved state, is noted $\hat{S}$ and computed using the following equation:

$$\hat{S} = [S_a^{-1} + K^T S_e^{-1} K]^{-1} \quad (2)$$

with S_e, the a priori covariance matrix of the measurement vector describing measurement/forward modelling uncertainties, and K, the Jacobian matrix containing the partial derivatives of the measurement with respect to the state vector parameters. Its elements are illustrated in the Supplements (see Fig. S1), for a usual SWIR spectrum and corresponding NanoCarb truncated interferogram.

Another useful OE result is the averaging kernel matrix, denoted A, which describes how the retrieved state $\hat{x}$ relate to the true – but unknown – geophysical state:

$$A = \frac{\partial \hat{x}}{\partial x} = \hat{S} K^T S_e^{-1} K \quad (3)$$

The diagonal elements of A are the state vector elements' degree of freedom, which provide a measure of the geophysical information obtained from the measurement through the OE process. Degrees of freedom close to 1 highlight a high contribution of the measurement in the estimation of a given state vector parameter, whereas degrees of freedom close to 0 denote a low contribution of the measurement and a high contribution of the a priori information. Finally, A also enables to compute the X_{CO_2} averaging kernel that describes its vertical sensitivity (Connor et al., 2008). It describes the atmospheric levels to which the retrieval is the most sensitive and it is essential to characterize and correctly exploit the retrieved X_{CO_2}.

3.2.2 Forward and inverse setups for performance evaluation

We use the 5AI inverse model (Dogniaux et al., 2021) that relies on 4A/OP radiative transfer model (Scott and Chédin, 1981) to build the Jacobian matrix K. These forward radiative transfer simulations rely on GEISA 2015 spectroscopic database (Jacquinet-Husson et al., 2016) with line-mixing effects for CO_2 (Lamouroux et al., 2015) and collision induced absorption in the O_2 0.76 µm band (empirical correction to Tran and Hartmann, 2008). Multiple scattering is taken into account through 4A/OP coupling with LIDORT (Spurr, 2002) and the aerosol optical properties are taken from the OPAC library (Hess et al., 1998). Finally, the atmospheric model is discretized in 20 atmospheric layers that bound 19 layers, as done by the ACOS algorithm (O'Dell et al., 2018).

We include in the state vector all the main geophysical variables necessary to model SWIR spaceborne measurements. Those are listed in Table 4, along with their a priori values and uncertainties. Finally, the measurement noise model that fills the diagonal of S_e is calculated, as in (Buchwitz et al., 2013), with a reference radiance L_{ref} and a reference signal-to-noise ratio SNR_{ref}:

$$\sigma_e = \begin{cases} L_{\mathrm{ref}}/SNR_{\mathrm{ref}}, \text{ if } L < L_{\mathrm{ref}} \\ L/\left(SNR_{\mathrm{ref}}\sqrt{L/L_{\mathrm{ref}}}\right), \text{ if } L \geq L_{\mathrm{ref}} \end{cases} \quad (4)$$

with σ_e, the noise model for a given spectral sample, and L, the radiance for a given spectral sample.

Table 4. State vector used for performance evaluation

Variable name	Length	A priori value	A priori uncertainty (1σ)	Notes
H_2O scaling factor	1	1.0	0.5	-
CO_2 profile	19 layers	394.95 ppm	Same matrix as ACOS (O'Dell et al., 2018)	-
Surface Pressure	1	1013.0 hPa	4.0 hPa	-
Temperature Profile Shift	1	0 K	5 K	-
Surface albedo (order 0 of albedo model)	1-4 bands	true synthetic value	1.0	4 bands in MicroCarb B1234 and NanoCarb cases
Surface albedo (order	1-4 bands	true synthetic	1.0	4 bands in MicroCarb B1234

1 of albedo model)		value		and NanoCarb cases Not included in the state vector for NanoCarb case.
Coarse mode aerosol Optical Depth (COD)	1 layer	0.02	0.1	-
Fine mode aerosol Optical Depth (COD)	1 layer	0.05	0.1	-

4 Results and discussion for CVAR

4.1 Impact of spectral resolution and signal-to-noise ratio

4.1.1 X_{CO_2} precision and degrees of freedom

For the atmospheric situation VEG-50º, Figure 3 shows the X_{CO_2} precision (or random error) and degrees of freedom (hereafter DOFs) as a function of both the resolving power $\lambda/\Delta\lambda$ and the signal-to-noise ratio (SNR) for CVAR, and for the exact CO$_2$M, MicroCarb and NanoCarb concepts (results for exactly-defined concepts are discussed in Sect. 5). The random error is computed from the a posteriori covariance matrix $\hat{S}$ given in Eq. (2), and the DOFs correspond to the sum of CO$_2$-related diagonal elements of matrix A, given in Eq. (3). As results change in values but conclusions do not for other albedo models and SZAs, figures that include all 12 atmospheric situations are shown in the Supplements.

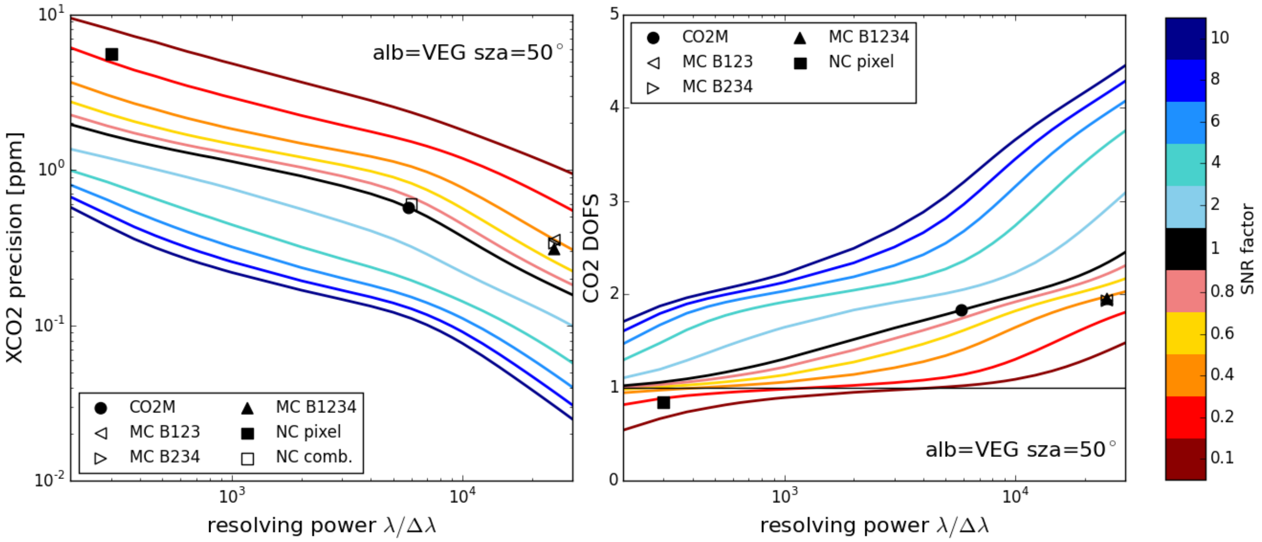

Figure 3. X_{CO_2} precision (left) and corresponding degrees of freedom for CO$_2$ (right), for the fictitious CVAR instrument for resolving power $\lambda/\Delta\lambda$ evolving from 200 to 30000 (horizontal axis), and for SNR evolving from 0.1 to 10 times CO$_2$M reference

SNR (colour scale), for the situation VEG-50°. Symbols give the same quantities for NanoCarb (NC, squares), MicroCarb (MC, triangles for various band combinations) and CO_2M (circle).

Results for the reference CO2M SNR are given by the black line. X_{CO_2} precision evolves from 1.96 ppm for $\lambda/\Delta\lambda$=200 to 0.16 ppm for $\lambda/\Delta\lambda$=30000. These values are consistent with those reported by previous studies: Galli et al. (2014) showed that degrading spectral resolution increased X_{CO_2} random errors (values cannot be compared because no real measurement is processed here) and Wu et al. (2020) reported an increase of mean X_{CO_2} retrieval noise from 0.25 ppm to 0.59 ppm (0.21 to 0.56 ppm in this work, respectively), when degrading OCO-2 measurements ($\lambda/\Delta\lambda$ ~ 20000) to CO2M-like resolving powers ($\lambda/\Delta\lambda$ ~ 6000). This improvement in precision with increasing resolving power is correlated to DOFs values that also increase with resolving power, from 1.02 to 2.45, respectively. Indeed, the more information a measurement can bring, the lower the X_{CO_2} random error. Changing the SNR has similar effects: the less noisy a measurement is, the more information it can carry, thus increasing SNR increases DOFs and reduces X_{CO_2} random error. For example, for $\lambda/\Delta\lambda$=6000 (close to CO2M resolution), X_{CO_2} precision evolves from 2.34 ppm to 0.11 ppm when multiplying SNR by 100. Overall, increasing the SNR by 2 orders of magnitudes improves the X_{CO_2} precision by a factor ranging from 16 to 37 (for increasing resolving powers), whereas increasing the resolving power by 2.2 orders of magnitude (from $\lambda/\Delta\lambda$=200 to $\lambda/\Delta\lambda$=30000) only improves X_{CO_2} precision by a factor ranging from 10 to 23 (for increasing SNR values). Hence, it appears that X_{CO_2} precision is more easily gained through SNR improvements rather than through resolving power improvements.

Furthermore, X_{CO_2} precision and DOFs grossly show two slope breaks (in logarithmic scale) as the resolving power $\lambda/\Delta\lambda$ increases. Depending on SNR, the first one occurs around $\lambda/\Delta\lambda$ ~ 400 – 1000. It corresponds to the complete P-R spectral band structure becoming visible, as previously commented for Fig. 2. Then, the second slope break occurs around $\lambda/\Delta\lambda$ ~ 4000 – 10000, it corresponds to the individual spectral lines of CO_2 becoming visible in spectral band branches, as also commented for Fig. 2. Interestingly, these slope breaks do not exactly occur for the same resolving power for different SNR values, and are more or less sharp. Indeed, the observation of band structures or individual spectral lines must be significant with respect to noise level to be actually able to bring information and improve X_{CO_2} precision. We note that these slope break occur for smaller resolving powers as SNR increases, and that DOFs and X_{CO_2} precision results for high SNR and low resolving powers correspond to results for low SNR and high resolving powers. Thus, a broad symmetry appears in the impact of SNR and resolving power on X_{CO_2} retrieval performance.

4.1.2 Vertical sensitivity: column averaging kernels

In addition to information content (given by DOFs and, symmetrically, by precision), the vertical sensitivity (or column averaging kernels, hereafter denoted AKs) of X_{CO_2} retrievals must be examined (see Sect. 3.2.1). Taking into account the vertical sensitivity of total columns is especially important when exploiting local column enhancements of verticallyinhomogeneous concentration increases. Indeed, any deviation from 1.0 in the vertical sensitivity wrongfully scales differences between the unknown truth and the prior into the retrieved column enhancement, thus calling for a posteriori corrections (e.g. Borchardt et al., 2021; Krings et al., 2011). Figure 4 shows AKs for CVAR with a resolving power varying from $\lambda/\Delta\lambda$ = 200 to 30000, and for three different scaling factors of CO$_2$M noise model (top row) and, conversely, shows AKs for scaling factors of CO$_2$M noise model varying from 0.1 to 10, and for three different resolving powers (bottom row). Figure 4 only includes results for the situation VEG-50º. Results for the other situations are shown in the Supplements. For low SNR and resolving power values, AKs reach their maximum in the atmospheric layer closest to the ground, and have near-zeros values at the top of the atmosphere. As SNR or resolving power (or both) increase, sensitivities for layers close to the ground improve, and become higher than one. For noise levels and a resolving power of about 6000 and above, the vertical sensitivity values are close to 1 from the ground surface up to approximately 300 hPa, and then decrease. For SNR and resolving power values even higher, AKs converge towards 1 for all atmospheric layers. Thus, as for their impact on X_{CO_2} precision or DOFs, the resolving power and noise level of an observing concept also have very similar impacts on AK shape for CVAR.

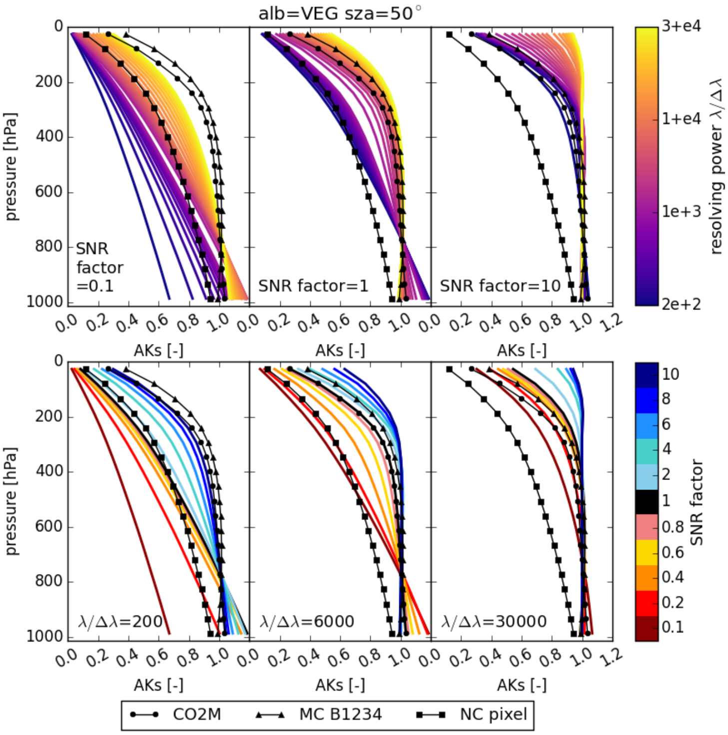

Figure 4. Vertical sensitivities (AKs) as a function of resolving power $\lambda/\Delta\lambda$ for three different SNR scaling factors (top), and as a function of SNR for three different resolving powers $\lambda/\Delta\lambda$ values (bottom), for the observational situation VEG-50º. Black lines with symbols give vertical sensitivities for CO$_2$M (circles), MicroCarb (triangles) and NanoCarb (squares).

https://doi.org/10.5194/amt-2023-233
Preprint. Discussion started: 14 November 2023

4.2 Impact of spectral resolution and spectral band selection

4.2.1 X_{CO_2} precision and degrees of freedom for CO₂ and interfering geophysical variables

For the atmospheric situation VEG-50º (results for other situations are given in the Supplements), Figure 5 shows the X_{CO_2} precision and DOFs as a function of both the resolving power $\lambda/\Delta\lambda$ and spectral band selection for CVAR (with SNR fixed at its reference value), and for the exact CO₂M, MicroCarb and NanoCarb concepts (results for exactly-defined concepts are discussed in Sect. 5). We can first note that including the O₂ 0.76 µm band (denoted B1 in Fig. 5) increases CO₂ DOFs for CVAR cases, compared to cases where it is not included (denoted B2, B3 and B23 in Fig. 5). This spectral band is indeed sensitive to surface pressure, temperature and aerosols, and can thus bring independent constraint on these geophysical parameters, which sensitivities also correlate with CO₂ sensitivity in 1.6 and 2.05 µm bands. For resolving powers above 1000, adding the O₂ 0.76 µm band has less impact on X_{CO_2} precision for B2 than for B3 cases. This may be explained by the fact that spectral lines are more saturated in B3, thus providing less information regarding the length of the optical path than in B2. Besides, we can also notice that CO₂ DOFs for B3/B13 are always higher than for B2/B12 cases. This may be explained by the fact that CO₂M 2.05 µm band includes two full sets of CO₂ P-R absorption branches (out of the three present near 2.05 µm, with one more saturated than the other, see Fig. 1), whereas there is only one set of CO₂ branches in B2 near 1.6 µm, for identical SNR values between B2 and B3. Thus, B3 carries more CO₂ information than B2. Interestingly, we can also notice that band configurations with the higher DOFs do not systematically translate into better X_{CO_2} precision: for example B3/B13 always shows higher DOFs than B2/B12, but very similar X_{CO_2} precisions from $\lambda/\Delta\lambda$=3000 and upwards. This is due to the covariance between CO₂ elements in the state vector that vary between band selection cases (see Supplements), which shows that different spectral bands carry different CO₂ information.

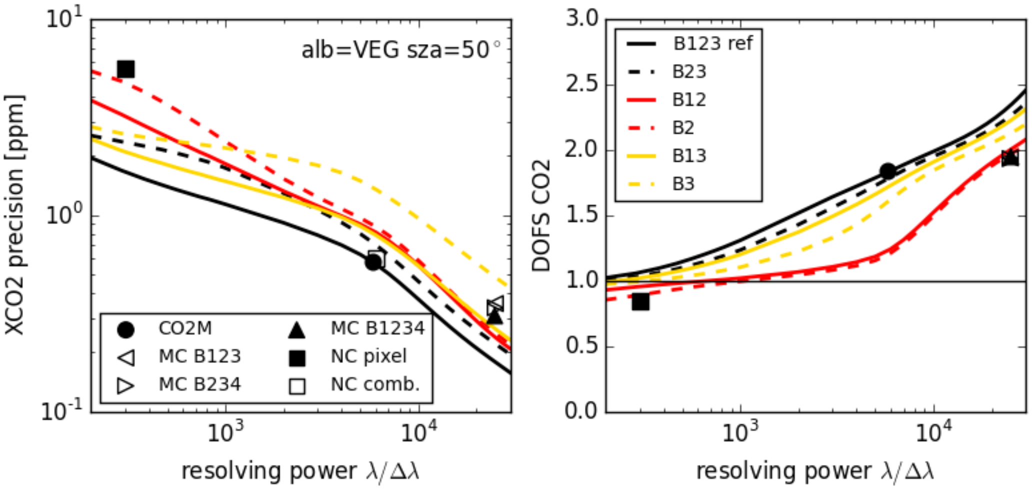

Figure 5. X_{CO_2} precision (left), and corresponding degrees of freedom for CO₂ (right), for the fictitious CVAR instrument for resolving power $\lambda/\Delta\lambda$ evolving from 200 to 30000 (horizontal axis), and for different spectral band selections: with and without O₂

0.76 µm band (B1, full and dashed-lines, respectively), with both CO_2 1.6 and 2.05 µm bands (B23, black), with only the 1.6 µm band (B2, red) and with only the 2.05 µm band (B3, yellow), for the situation VEG-50°. Symbols give the same quantities for NanoCarb (NC, squares), MicroCarb (MC, triangles for various band combinations) and CO_2M (circle).

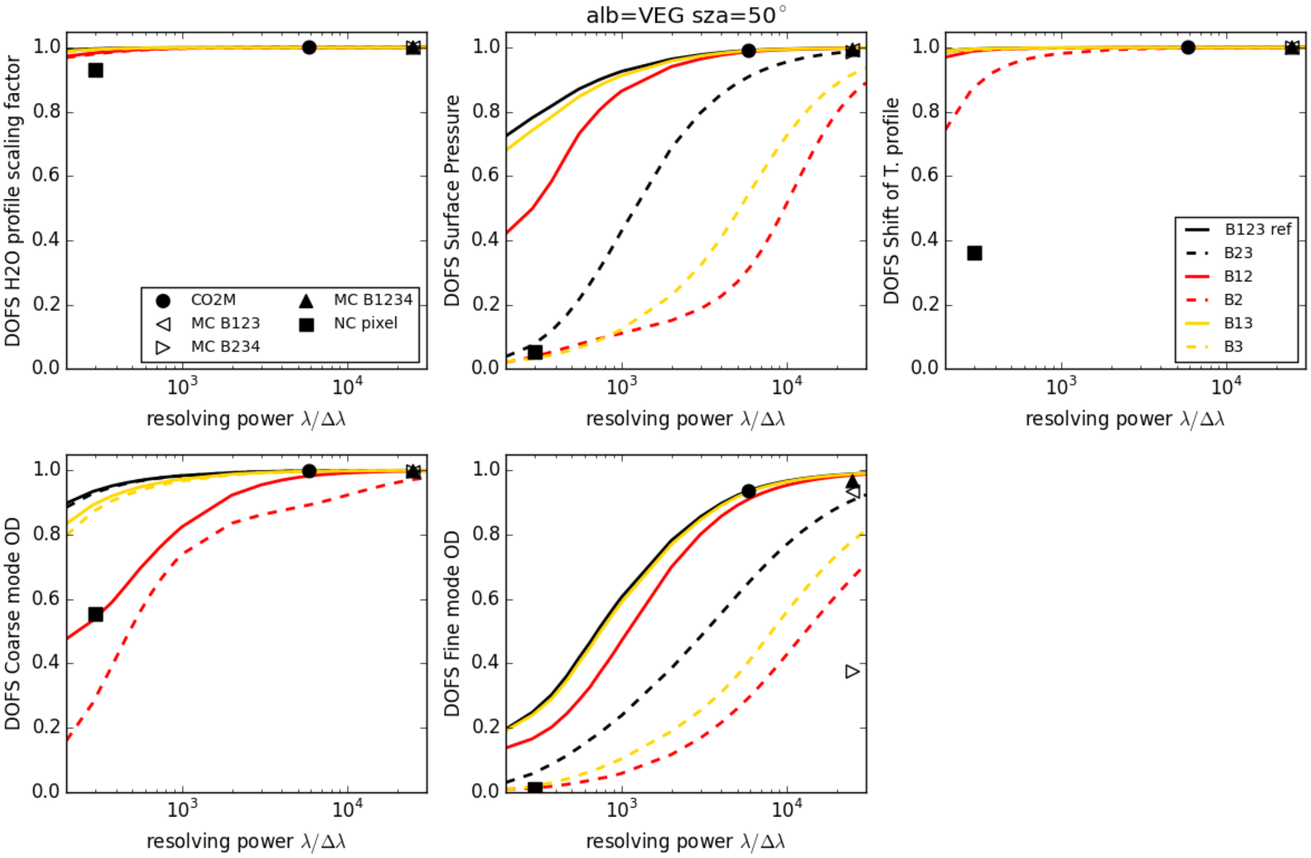

Figure 6. Degrees of freedom for H2O scaling factor (top, left), Surface pressure (top, center), Temperature profile shift (top, right), Coarse mode aerosol optical depth (bottom, left) and Fine mode aerosol optical depth (bottom, center), for the fictitious CVAR instrument for resolving power $\lambda/\Delta\lambda$ evolving from 200 to 30000 (horizontal axis), and for different spectral band selections: with and without O_2 0.76 µm band (B1, full and dashed-lines, respectively), with both CO_2 1.6 and 2.05 µm bands (B23, black), with only the 1.6 µm band (B2, red) and with only the 2.05 µm band (B3, yellow), for the situation VEG-50°. Symbols give the same quantities for NanoCarb (NC, squares), MicroCarb (MC, triangles for various band combinations) and CO_2M (circle).

For the atmospheric situation VEG-50° (results for other situations are given in the Supplements), Figure 6 completes Fig. 5 by showing DOFs for interfering geophysical variables (H_2O profile scaling factor, surface pressure, temperature profile shift and aerosol optical depths; albedo-related parameters are not included because they are all very close or equal to 1) as a function of both the resolving power $\lambda/\Delta\lambda$ and spectral band selection for CVAR (with SNR fixed at its reference value), and for the exact CO_2M, MicroCarb and NanoCarb concepts (see Sect. 5). For all five variables, DOFs increase with resolving powers and tend towards 1. H_2O profile scaling factor and temperature profile shift exhibit high close-to-one DOFs for almost all resolving powers and spectral band selection cases in the configuration used here. Surface pressure and aerosol optical depths, variables that influence the length of the optical path, have more sensitivity to resolving power, and also especially to the inclusion – or not – of the O_2 0.76 µm band (B1) in the spectral band selection. Cases that do not include B1 show much lower DOFs for these variables, illustrating once again, how useful this band is to constrain interfering geophysical variables. This result is made possible by the (usual) hypothesis of fixed aerosol optical properties, which enables sharing optical path information across spectral bands. Overall, we can also note that, for all geophysical variables, DOFs for B13 are more or less significantly closer to those of B123, compared to DOFs of B12. This shows that the CO_2 1.6 µm band only brings little complementary interfering variable information on the top of the one already carried by the 2.05 µm band.

Previous studies that have explored the impact of spectral band selection and/or spectral resolution on X_{CO_2} performance provide conclusions in broad agreement with the previously presented results. Wilzewski et al. (2020) studied the performance of X_{CO_2} retrievals from spectrally-degraded GOSAT measurements only using the 1.6 or 2.05 µm spectral bands. While methodologies are hardly comparable (because this study is only based on synthetic simulations), both works agree that a sharp change in how X_{CO_2} precision evolves with resolving power is to be expected around $\lambda/\Delta\lambda$ = 1000 – 2000, when solely using the 1.6 or 2.05 µm CO_2 bands (see Supplements for Fig. 5 plotted in linear scale). Building on Wilzewski et al. (2020), Strandgren et al. (2020) select the 2.05 µm CO_2 band for the design of a moderate resolution instrument, partly because it shows scattering particle sensitivity. Results presented here are consistent with this conclusion: using the sole 2.05 µm band yields higher (or equal for surface pressure at low resolving powers) DOFs for all geophysical variables, compared to using the sole 1.6 µm CO_2 band.

4.2.2 Vertical sensitivity: column averaging kernels

Figure 7 gives the column averaging kernel – which describe X_{CO_2} vertical sensitivity – for all CVAR spectral band selection cases, and for three different resolving power values (200, 6000 and 30000). For lower resolving powers, spectral band selection cases that include the CO_2 2.05 µm band (B3) show a greater sensitivity to atmospheric levels close to the surface. This may be explained by the fact that this spectral band includes saturated spectral lines which are more sensitive to CO_2 concentration variations in atmospheric layers close to the surface, as it can be seen for example in Fig. 2 in (Roche et al., 2021). As for Fig. 4, AKs tend to converge towards unity when resolving power increases, and this difference between bands disappears. Besides, it can be noted that, comparing AKs between B23 and B123 spectral band selection cases, including or not an O_2 sensitive band does not have a strong impact on X_{CO_2} vertical sensitivity.

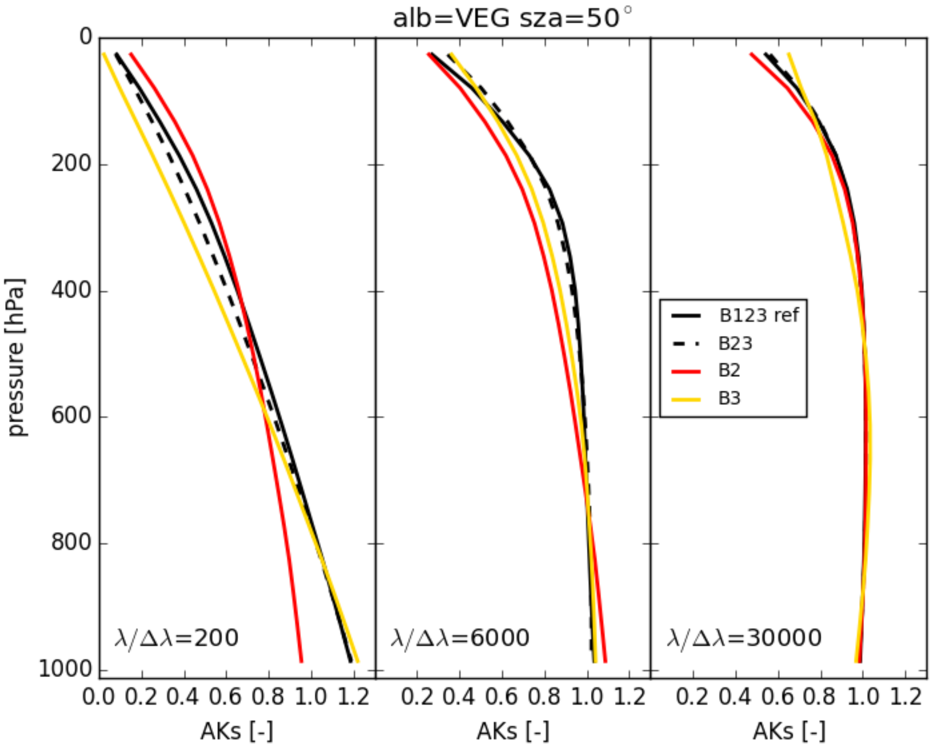

Figure 7. Vertical sensitivities (AKs) for different spectral band selections (colours and line styles, see legend), and three different resolving powers $\lambda/\Delta\lambda$ values, for the observational situation VEG-50º.

4.2.3 Geophysical information entanglements

Geophysical information is more or less entangled in SWIR measurements (as illustrated for example by a posteriori correlation matrices shown in the Supplements S15 or in Fig. 10), depending on the measurement nature (spectra or truncated interferogram), and also on its characteristics (spectral band selection, spectral resolution, SNR, etc.). One consequence of these entanglements is that possible a priori misknowledge of the atmospheric state can impact retrieved X_{CO_2} and cause biases: this is called smoothing error (Connor et al., 2008; Rodgers, 2000). In this section, we use the averaging kernel matrix A to propagate a priori misknowledge of the synthetic true state of the atmosphere for non-CO_2 interfering variables in order to evaluate its impact on retrieved X_{CO_2}. Figure 8 shows, for the 12 atmospheric and observational situations considered in this work, the X_{CO_2} impact of a priori misknowledge for several state vector variables for all CVAR spectral band selection cases, for resolving power values ranging from 200 to 30000, as well as for the exact MicroCarb, CO_2M and NanoCarb concepts (see Sect. 5 for exactly-defined concepts). These a priori perturbations include: (1) +10% to H_2O profile scaling factor; (2) + 1 hPa to surface pressure; (3) + 1 K to the temperature profile shift; and (4)

+0.05 to the albedo in 1.6 µm band. All situations and perturbations are sorted along a unique axis, and the top three panels in Fig. 8 describe both the situations (albedo and SZA) and perturbations considered.

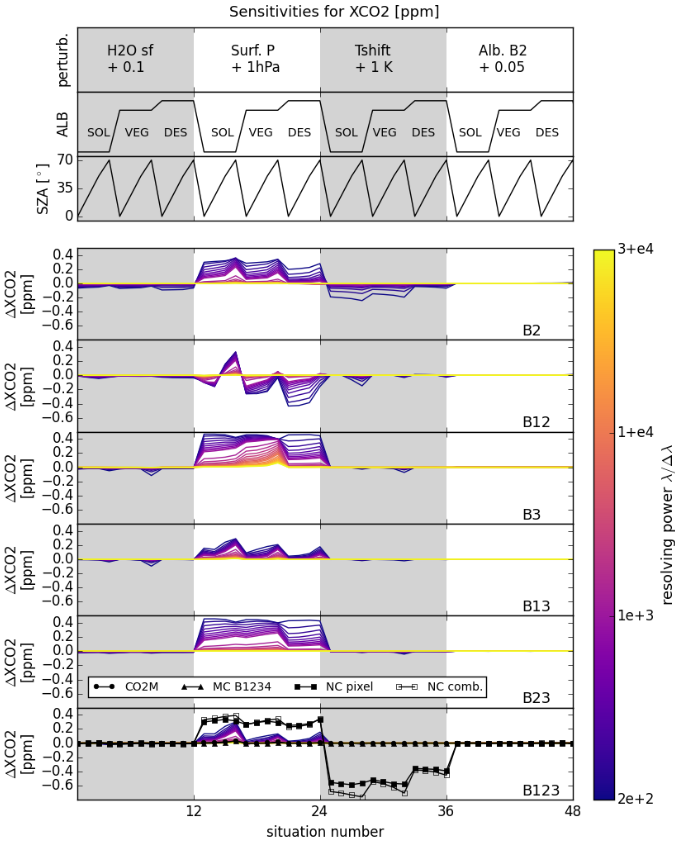

Figure 8. $\boldsymbol{X_{CO_2}}$ **sensitivities (noted** $\boldsymbol{\Delta X_{CO_2}}$**) to prior misknowledge of water vapor, surface pressure, temperature profile shift and 1.6 µm band albedo value (described in the top panel), for 12 observational situations (described in the 2nd and 3rd panels), for 6 different CVAR spectral band selections (lines in the 6 bottom panels) and resolving power values ranging from 200 to 30000 (color scale). Black lines with symbols give the same sensitivities for CO$_2$M (circles), MicroCarb (triangles) and NanoCarb (squares) in the bottom panel.**

First, regarding water vapour, X_{CO_2} sensitivities are very small for all CVAR band selection configurations (consistently with results in Fig. 6), spectral resolutions and exactly described concept: for VEG-70º in CVAR B3 case, for the lowest resolving power, it amounts to a maximum of 0.12 ppm, in absolute value. This means that if a water vapor plume is correlated with a CO$_2$ emission plume, in the exhaust fumes of a coal-fired power plant for instance, a small bias in retrieved X_{CO_2} enhancement could then hamper estimations from a low resolving power (but potentially high spatial resolution) instrument. However, considering that emission rates computed from enhancements with mass-balance approaches may have uncertainties up to 65% (mainly due to wind-speed errors, Varon et al., 2018), this sensitivity of retrieved X_{CO_2} to water vapour appears insignificant.

Regarding surface pressure, X_{CO_2} sensitivities are close to zero for all resolving powers above 10000, and increase differently depending on spectral band selection case for lower resolving powers. They reach up to 0.47 ppm for CVAR B3 case at the lowest resolving power value tested. Overall, X_{CO_2} sensitivities to prior surface pressure misknowledge is reduced when the O_2 0.76 µm band is included in the measurement, consistently with results shown in Fig. 6. These sensitivities can be expected to impact the full-swath of an imaging instrument with lower resolving powers, and thus can be removed when computing an enhancement. However, they would blindly impact observations without emissions plumes to detect, thus making these observations hard to exploit for other purposes than anthropogenic point source monitoring.

Regarding temperature global shift, consistently with high DOFs shown in Fig. 6, X_{CO_2} sensitivities are overall very small for spectral resolving power above 1000 and all CVAR spectral band selection cases. For resolving powers lower than 1000, they can reach up to 0.23 ppm in absolute value, for the CVAR B2 case for instance (see lower DOFs in Fig. 7).

Finally, all cases and concepts exhibit near-zero (or even, by construction, exactly-zero for B3 and B13 CVAR cases) X_{CO_2} sensitivities when perturbating the 1.6 µm CO_2 band albedo by 0.05. This reflects the albedo DOFs very close or equal to 1 that we obtain with this inverse setup configuration, as well as the low posterior correlations between albedo and CO_2 parameters in the state vector.

4.2.4 Focus on sensitivities to prior aerosol misknowledge

We follow the approach used for NanoCarb performance assessement (Dogniaux et al., 2022), that was first introduced by Buchwitz et al. (2013) for the performance assessment of CarbonSat. Considering the previously described 12 atmospheric and observational situations that span three different albedo models and four SZA values, we explore the X_{CO_2} sensitivities for synthetic coarse mode aerosol optical depths spanning 0.001 – 0.15 (with a fixed prior of 0.02) and fine mode aerosol optical depths spanning 0.001 – 0.22 (with a fixed prior of 0.05), thus yielding 192 situations in total. This a priori misknowledge of aerosol optical depths is propagated through the averaging kernel matrix A to evaluate its impact on retrieved X_{CO_2} values.

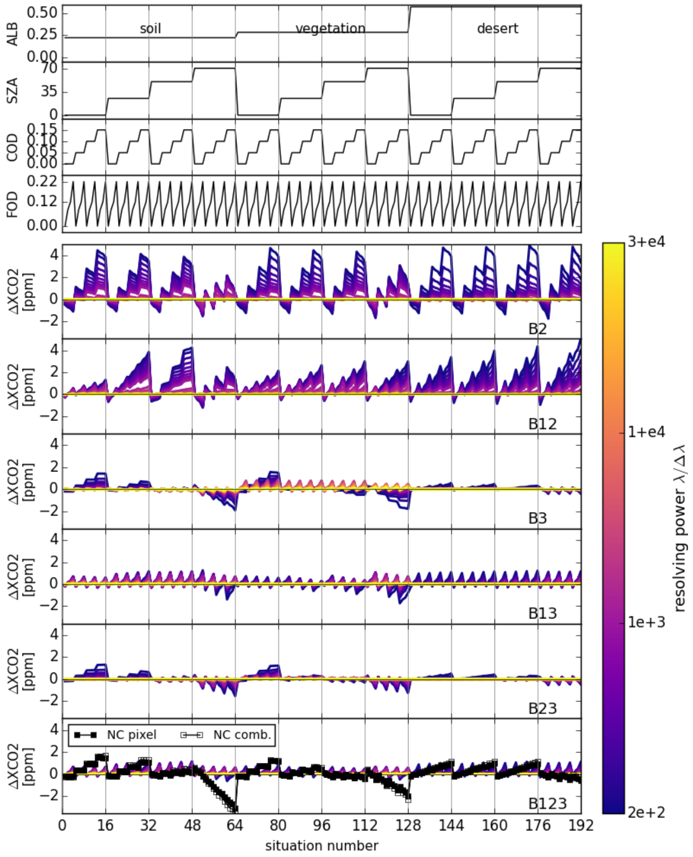

Figure 9. X_{CO_2} sensitivities (noted ΔX_{CO_2}) to prior misknowledge of aerosol optical depths (described in the 3rd and 4th top panels), for 12 observational situations (described in the 1st and 2nd panels), for 6 different CVAR spectral band selections (lines in the 6 bottom panels) and resolving power values ranging from 200 to 30000 (color scale). Black lines with symbols give the same sensitivities for NanoCarb (squares) in the bottom panel.

Figure 9 shows for the 192 considered situations, the X_{CO_2} impact of a priori aerosol optical depth misknowledge for all CVAR spectral band selection cases, for resolving power values ranging from 200 to 30000, as well as for the exact NanoCarb concept (results for NanoCarb are discussed in Sect. 5). All situations are sorted along a unique axis, and the top four panels in Fig. 9 describe a given situation (albedo and SZA, coarse and fine mode optical depths).

For CVAR B2 and B12 cases, X_{CO_2} sensitivities at low resolving powers reach up to about ~5 ppm. They mostly correlate with a priori misknowledge of coarse mode aerosol optical depth, and secondarily to fine mode aerosol optical depth, and diminish as spectral resolving power increases. Sensitivities are also different depending on albedo model and SZA values, thus reflecting that the information content carried by a given measurement also depends on the scene (see DOFs for all situations in the Supplements). Including the O_2 0.76 µm band in addition to the CO_2 1.6 µm band reduces X_{CO_2} sensitivities to a priori aerosol misknowledge at low SZA values for low resolving powers, but show low or even detrimental impacts at higher SZAs.

Unlike CO_2 1.6 µm band, the CO_2 2.05 µm band carries more aerosol information and thus results for CVAR B3 and B13 selection cases show lower impacts of these variables on X_{CO_2} retrievals, with a maximum of ~2 ppm in absolute value. For CVAR B3 case, X_{CO_2} sensitivities to a priori aerosol misknowledge are mostly correlated to coarse mode misknowledge for low resolving powers and to fine mode misknowledge for higher resolving powers, converging towards near-zero values for the highest resolving powers. Interestingly, including the O_2 0.76 µm band changes this correlation pattern and X_{CO_2} sensitivities appear to be mostly correlated to fine mode aerosol misknowledge for B13 case, with slightly higher X_{CO_2} sensitivities compared to B3 case for some situations, such as those with soil or desert-like albedo.

Results for B23 and B123 mostly follow the patterns showed by B3 and B13 cases (as B3 brings most of the aerosol information compared to B2), only with slightly lower X_{CO_2} sensitivity values, reflecting the little complementary information brought by B2 on the top of B3.

5 Results and discussion for exactly-defined concepts: CO_2M, MicroCarb and NanoCarb

5.1 X_{CO_2} precision and degrees of freedom

Besides results for CVAR, Fig. 3 also includes the performance computed for three explicit concepts: the upcoming CO_2M and MicroCarb missions, as well as the NanoCarb concept that is currently being studied. CO_2M shows an X_{CO_2} precision of 0.56 ppm, which is consistent with the 0.7 ppm precision requirement for a vegetation scene with SZA=50º given in (Meijer, 2020). For MicroCarb (MC1234, when including the 4 spectral bands), we find an X_{CO_2} precision of 0.31 ppm that satisfactorily compares to the median 0.35 ppm contribution of SNR to the mission error budget (with the full range of possible contribution being 0.15 – 0.94 ppm, personal communication). Besides, we can notice that removing one of the two O_2-sensitive spectral band from MicroCarb measurement slightly decreases precision (MC123 for 0.76-1.6-2.05 µm bands, and MC123 for 1.6-2.05-1.27 µm bands). Indeed, less geophysical information is available to help constrain interfering variables. Finally, MicroCarb (MC1234) shows only slightly higher CO_2 DOFs compared to CO_2M despite having a spectral resolution 5 times higher: this may be explained by the fact that their respective spectral bands are not covering the same wavelength intervals, as it can be seen in Fig. 1.

Two different X_{CO_2} precision results are included for NanoCarb in Fig 3.: one given for a unique pixel located at the FOV centre (filled square), and another one obtained after combining results acquired from different viewing angles as the two-dimensional FOV of NanoCarb flies over a scene (see Sect 2.3 or the extensive description in Dogniaux et al., 2022). For a unique observation of a given scene, performed by the FOV central pixel, NanoCarb yields a precision of 5.6 ppm. However, after combining the maximum 102 observations (over different viewing angles) of the same scene, NanoCarb random error is reduced to 0.60 ppm, which is close to CO_2M performance. It must be noted that, because of its very nature, NanoCarb does not have a spectral resolution per se. Thus, we arbitrarily attributed a resolving power of $\lambda/\Delta\lambda = 300$ to plot NanoCarb pixel-wise performance, and a resolving power $\lambda/\Delta\lambda = 6000$ to plot NanoCarb performance for combined pixels. This choice enables to highlight that NanoCarb pixel-wise performance compares to concepts measuring spectra at low spectral resolution and low SNR, whereas once retrieval results from observations that are assumed independent are combined, the X_{CO_2} precision compares to CO_2M.

However, despite similar precisions, further comparisons enable to exhibit how their respective X_{CO_2} observations are not equivalent. Indeed, we can first notice that their respective DOFs are not comparable at all: CO_2M shows 1.83 DOFs for CO_2, whereas NanoCarb pixel-wise CO_2 DOFs amount to 0.85 (no averaging kernel matrix is computed for NanoCarb combined-pixel results, as performance is evaluated per pixel and the combination then assumes that they are independent). These low CO_2 DOFs for NanoCarb are explained by the low CO_2 information content of NanoCarb measurement (compared to concepts that measure spectra), and its entanglement with other geophysical variable information, as mentioned in Dogniaux et al. (2022). One can indeed notice that CO_2 and other variable Jacobians are correlated (see Fig S1 in the Supplements): this makes it harder for OE to yield independent estimates for CO_2 and other parameters.

An other way to look at this issue is to consider a posteriori correlations between state vector parameters, as given by the a posteriori covariance matrix $\hat{S}$. Pearson correlation coefficient matrices computed from $\hat{S}$ are shown for CO_2M, MicroCarb (MC1234) and NanoCarb in Fig. 10. First, regarding CO_2 profile, we notice the very high positive correlation between different atmospheric layers for NanoCarb, compared to CO_2M and MicroCarb cases. This is a result of the low CO_2 information content in NanoCarb measurements, compared to CO_2M and MicroCarb. Besides, in this state vector configuration, NanoCarb a posteriori covariance matrix shows stronger correlation between CO_2 atmospheric layers and Temperature profile shift than for CO_2M and MicroCarb. A slight positive correlation between CO_2 atmospheric layers and albedo parameters can also be noted for NanoCarb, unlike CO_2M and MicroCarb that show small negative correlations. The close-to-1.0 correlation between albedo parameters of different bands are due to the presence of aerosol optical depth parameters in the state vector (assuming fixed aerosol optical properties). When aerosol optical depths are removed from the state vector, these correlations between albedo parameters of different bands decrease (see Supplements S16). Interestingly, in that case, correlations between CO_2 atmospheric layers and albedo parameters reach up to 0.6 for NanoCarb, whereas they reach 0.2 and 0.1 for CO_2M and MicroCarb, respectively (see Supplements). Thus, all things considered, NanoCarb contains less geophysical information than other concepts that measure spectra, and such a comparison helps pave the way for future improvement of the NanoCarb concept.

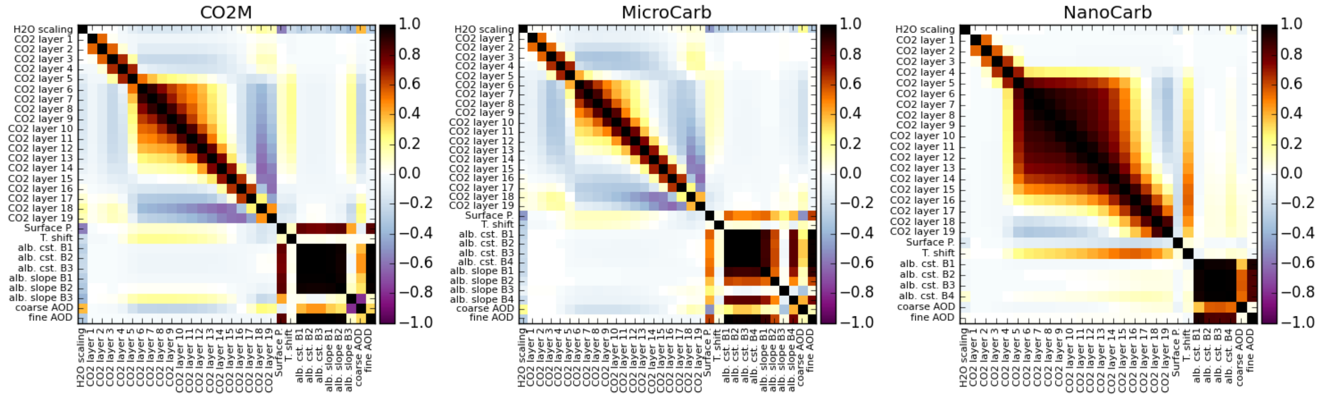

Figure 10. A posteriori correlation matrices for CO_2M (left), MicroCarb (center) and NanoCarb (right), for the VEG-50° situation.

5.2 Vertical sensitivity: column averaging kernels

Besides results for CVAR, Fig. 4 also includes the vertical sensitivities of CO_2M or MicroCarb and NanoCarb. Thanks to their spectral resolution and SNR, CO_2M and MicroCarb show vertical sensitivities that are close to 1 from the surface to about 300 hPa, and that then decrease. Interestingly, NanoCarb AKs do not exactly share the shape of CVAR, CO_2M or MicroCarb AKs. For the atmospheric layers closest to the ground, NanoCarb AK follows the AK shape of an instrument with low resolving power and SNR (consistently with how NanoCarb single-pixel performance compares to CVAR in Fig. 3). For higher up atmospheric layers, it follows the AK shape of an instrument with medium resolving power and low SNR, or vice versa.

5.3 Non-CO_2 degrees of freedom

Besides results for CVAR, Fig. 6 also gives interfering variable DOFs for the exact CO_2M, MicroCarb and NanoCarb concepts. For MicroCarb and CO_2M, DOFs for H_2O profile scaling factor, surface pressure, temperature global shift and coarse mode aerosol optical depth are all nearly equal to 1. Only for fine mode aerosol optical depth do DOFs appear to be – slightly – lower than 1, with the exception of MicroCarb B234 configuration test, where fine mode DOF is close to 0.4. This shows that different optical path length information is carried depending on whether the O_2 0.76 µm or 1.27 µm bands are used. NanoCarb exhibits near-zero DOFs for surface pressure and fine mode optical depth in this retrieval configuration, as well as non-zero yet rather low DOF values for H_2O profile scaling factor, temperature global shift and coarse mode aerosol optical depth (0.93, 0.36 and 0.55, respectively).

https://doi.org/10.5194/amt-2023-233
Preprint. Discussion started: 14 November 2023

5.4 Geophysical information entanglements

Besides results for CVAR, Fig. 8 also gives CO$_2$M, MicroCarb and NanoCarb X_{CO_2} sensitivities to a priori misknowledge of water vapour, surface pressure, temperature profile, and 1.6 µm albedo. These X_{CO_2} sensitivities are close to zero for MicroCarb and CO$_2$M, for the four tested geophysical variables.

Prior misknowledge of surface pressure reach up to 0.39 ppm for NanoCarb, showing again results comparable to low spectral resolution instruments. Sensitivities for NanoCarb central pixel (filled squares) and NanoCarb combined results for the central row of pixels (empty squares) slightly differ because information entanglement evolves depending on the pixel location in the NanoCarb FOV. NanoCarb also shows significant X_{CO_2} sensitivities to a priori temperature misknowledge that reach -0.76 ppm, consistently with the strong correlation shown between the temperature profile shift and CO$_2$ related parameters in the state vector (see Fig. 10). This result is not surprising as the version of the NanoCarb concept used in this work did not consider the possible impact of entanglements between CO$_2$ and temperature (see Sect 2.3 or Dogniaux et al., 2022; Gousset et al., 2019). This paves the way for future improvements of this very compact instrumental concept.

Regarding the sensitivity to prior aerosol misknowledge, Fig. 9 also shows results for the exact NanoCarb concept, for both the central FOV pixel and the combination of the central along-track row of pixels. For SZA values lower or equal to 50º (in soil and vegetation albedo situations) and for all SZAs in desert albedo situations, those mostly correlate with coarse mode aerosol misknowledge, and reach absolute values up to 1.7 ppm. For SZA=70º in soil and vegetation albedo situations, NanoCarb aerosol DOFs not only increase (see Fig. S13-14 in Supplements), but correlations between CO$_2$ and aerosol state variables also increase by a lot (see Fig. S17 in Supplements), thus leading to the larger sensitivities shown in Fig. 9 (or Fig. 11). This illustrates that different surface types and SZA must be explored for thorough performance assessments.

Figure 11 is similar to Fig. 9, but focuses on the exact concepts studied of CO$_2$M and MicroCarb. Their X_{CO_2} sensitivities to prior aerosol optical depth misknowledge is overly correlated to the one of fine mode optical depth. It can be explained by the fact that their coarse mode optical depth DOFs are very close to 1, thus enabling a correct estimation (in this synthetic simulation set up) of this geophysical parameter, which results in a very low impact of coarse mode optical depth misknowledge on X_{CO_2} retrievals. However, their fine mode DOFs are below 1, thus leading to estimation errors that impact X_{CO_2} retrievals through a posteriori correlations (see Fig. 10 or Supplements S17). Overall, CO$_2$M shows sensitivities up to 0.2 ppm, with maximums reached for the SOL-25º situation. These values are well below the 0.5 ppm systematic error requirement (Meijer, 2020), and are expected to be even more reduced by using the aerosol observations provided by the Multi-Angle Polarimeter that will fly along CO$_2$M spectrometers (e.g. Rusli et al., 2021). As for MicroCarb, its X_{CO_2} sensitivities to aerosol optical depth misknowledge measurement peak for soil-albedo situations up to about 0.6 ppm when just including the 0.76 µm O$_2$ band (B123), and up to 0.1 ppm when both 0.76 and 1.27 µm O$_2$ bands are included (B1234), whereas it peaks up to -0.2 ppm for vegetation-albedo situations when only the 1.27 µm O_2 band is available (B234). Interestingly, sensitivities for MicroCarb B123 and B1234 are positively correlated to fine mode aerosol optical depth values, whereas MicroCarb B234 are negatively correlated. This illustrates that the O_2 1.27 µm band carries complementary optical path length information compared to the O_2 0.76 µm band (see also a posteriori correlation matrices in Supplements S17).

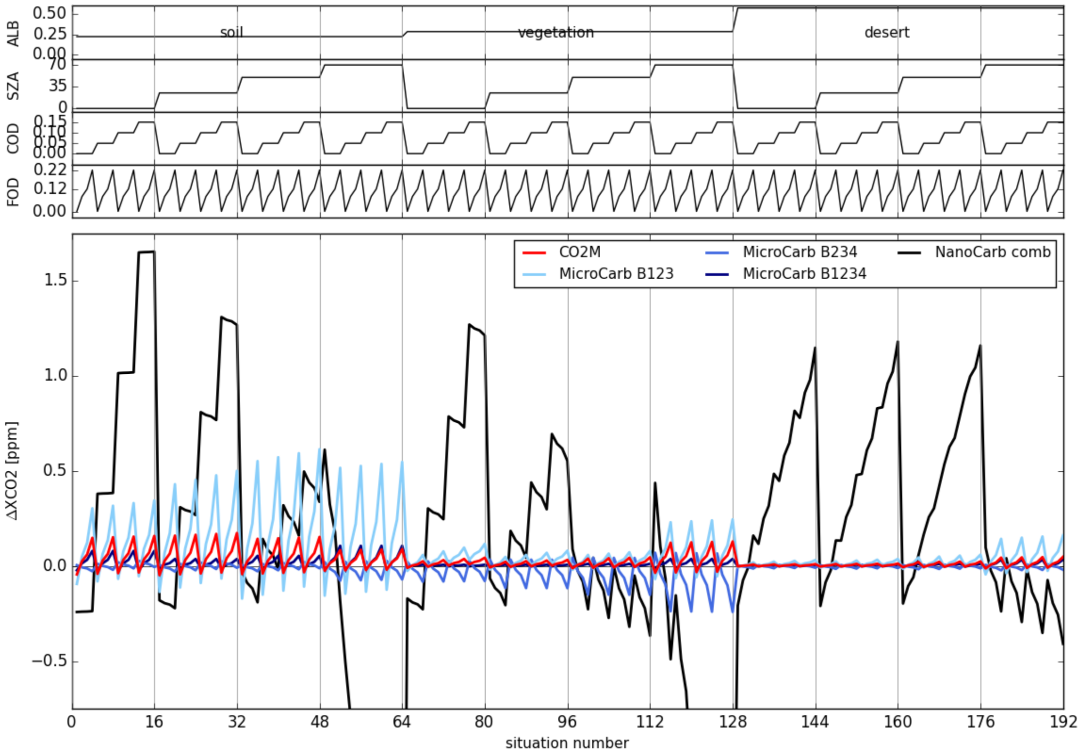

Figure 11. Same as Fig. 10, but containing only results for CO_2M, MicroCarb and NanoCarb.

6 Conclusions

In this work, we have carried out a synthetic survey that describes the impact of measurement design choices on X_{CO_2} retrieval performance, for shortwave infrared (SWIR) satellite observations. In order to be representative of the large extent of upcoming concept designs, it explored – for a fictitiously-varying CO_2M-like instrument – the impact of three different parameters: (1) spectral resolution; (2) signal-to-noise ratio, for values spanning two orders of magnitude, and (3) spectral band selection within the measurement. In addition, three exactly-defined concepts have been consistently studied: CO_2M, MicroCarb and NanoCarb.

https://doi.org/10.5194/amt-2023-233
Preprint. Discussion started: 14 November 2023

First, X_{CO_2} precision and CO_2 information content of SWIR measurements improve when increasing either or both resolving power and signal-to-noise ratio. For CO_2M-like SNR values, increasing the resolving power by 2.2 orders of magnitude enables to improve precision by a factor of about 12, from 1.90 ppm down to 0.16 ppm. These results show two critical turns in how precision or CO_2 DOFs evolve with spectral resolution: the first one corresponds to the spectral resolution enabling to distinguish the CO_2 P-R spectral band structure, and the second to the spectral resolution enabling to resolve individual CO_2 spectral lines. For a resolving power of 6000, multiplying SNR by 100 enables to improve precision by a factor of about 21, from 2.34 ppm down to 0.11 ppm. Overall, precision is more easily gained through SNR improvement than through spectral resolution improvements. The separate impacts of these two parameters show a broad symmetry in precision, as well as in vertical sensitivities: measurements with lower SNR and/or spectral resolution give more weight to atmospheric layers close to the surface for the retrieved total columns.

The comparison of different spectral band selections included in a SWIR measurement provided two main conclusions. First, including the O_2 0.76 µm band strongly increases information content for parameters impacting the optical path length (for all resolving powers), and helps to noticeably reduce the impact of a priori misknowledge of these parameters on retrieved X_{CO_2} values. Secondly, the CO_2 2.05 µm band (and especially for coarse aerosol mode) carries overall more information than the 1.6 µm band, and thus seems more appropriate for concepts that measure a single CO_2-sensitive spectral band, especially at low to mid-spectral resolution values. This is reflected in X_{CO_2} sensitivities to a priori misknowledge of different state parameters shown by concepts with the CO_2 2.05 µm, for low to mid-resolving power values: they are overall lower than those that just include the 1.6 µm band only.

The exact CO_2M, MicroCarb and NanoCarb concepts were also studied in addition to the fictitiously-varying ones. With an about 5-times higher spectral resolution but shorter spectral band intervals, MicroCarb shows slightly higher CO_2 DOFs compared to CO_2M, and its X_{CO_2} precision is lower by a factor ranging from about 1.1 to 1.9, depending on observational situations. Their vertical sensitivities are very similar, and their DOFs for other interfering variables are mostly very close to 1, with the exception of fine aerosol mode, where they show slightly lower values. Besides, MicroCarb exhibits varying information content on optical path length related variables, depending on whether the 0.76 µm and/or the 1.27 µm O_2 sensitive bands are included in the calculations. Regarding NanoCarb, that only measures truncated interferograms and not full spectra, its pixel-wise X_{CO_2} performance compares on many aspects to the performance of low spectral resolution and low-SNR spectra-observing concepts. However, the X_{CO_2} precision obtained after combining several observations of the same location is close to CO_2M X_{CO_2} precision. The comparison between NanoCarb DOFs and those of spectra-measuring concepts (regardless of its characteristics) highlights that further improvements of the concept are needed, to increase its information content for interfering geophysical variables.

This new opening decade will see a large increase in spaceborne monitoring of X_{CO_2} from a wide variety of SWIR-observing concepts. While this study could not obviously address the whole extent of possible design parameters (e.g. band-wise variations of spectral sampling ratios, varying wavelength interval for spectral bands, combination of different instruments, etc.), it has however enabled to explore three of the most critical parameters, and it already shows how different we can expect upcoming X_{CO_2} products will be, in their respective performance and sensitivities to interfering variables. This hints at the extent of work that will be required to compare, reconcile and cross-calibrate the results produced by so many different satellites concepts, especially if their purpose is to support independent evaluation of mitigation efforts aiming at Paris Agreement objectives.

Data availability

The outputs of radiative transfer simulations and scripts to generate synthetic performance results are available from Matthieu Dogniaux upon request by email (M.Dogniaux@sron.nl).

Author contributions

MD designed this study, and carried it out with the help and supervision of CC. MD wrote this article with feedback from CC.

Competing interests

The authors declare that they have no conflict of interest.

Financial support

MD was funded by Airbus Defence and Space in the framework of a scientific collaboration with École polytechnique. This work has received funding from CNES and CNRS. The Space CARBon Observatory (SCARBO) project, that supported NanoCarb development, received funding from the European Union’s H2020 research and innovation program under grant agreement No 769032.

Acknowledgements

The authors are thankful for the funding received from Airbus Defence and Space, CNES and CNRS, and grateful to Raymond Armante and Vincent Cassé for their helpful comments and proof-reading of this manuscript.

References

Baldridge, A. M., Hook, S. J., Grove, C. I. and Rivera, G.: The ASTER spectral library version 2.0, Remote Sens. Environ., 113(4), 711–715, doi:https://doi.org/10.1016/j.rse.2008.11.007, 2009.

Bertaux, J.-L., Hauchecorne, A., Lefèvre, F., Bréon, F.-M., Blanot, L., Jouglet, D., Lafrique, P. and Akaev, P.: The use of the 1.27\,\unit{\mu}m \chem{O_2} absorption band for greenhouse gas monitoring from space and application to MicroCarb, Atmos. Meas. Tech., 13(6), 3329–3374, doi:10.5194/amt-13-3329-2020, 2020.

Boesch, H., Baker, D., Connor, B., Crisp, D. and Miller, C.: Global Characterization of CO2 Column Retrievals from Shortwave-Infrared Satellite Observations of the Orbiting Carbon Observatory-2 Mission, Remote Sens., 3(2), 270–304, doi:10.3390/rs3020270, 2011.

Borchardt, J., Gerilowski, K., Krautwurst, S., Bovensmann, H., Thorpe, A. K., Thompson, D. R., Frankenberg, C., Miller, C. E., Duren, R. M. and Burrows, J. P.: Detection and quantification of CH$_4$ plumes using the WFM-DOAS retrieval on AVIRIS-NG hyperspectral data, Atmos. Meas. Tech., 14(2), 1267–1291, doi:10.5194/amt-14-1267-2021, 2021.

Bovensmann, H., Burrows, J. P., Buchwitz, M., Frerick, J., Noël, S., Rozanov, V. V., Chance, K. V. and Goede, A. P. H.: SCIAMACHY: Mission objectives and measurement modes, J. Atmos. Sci., 56(2), 127–150, doi:10.1175/1520-0469(1999)056<0127:SMOAMM>2.0.CO;2, 1999.

Bovensmann, H., Buchwitz, M., Burrows, J. P., Reuter, M., Krings, T., Gerilowski, K., Schneising, O., Heymann, J., Tretner, A. and Erzinger, J.: A remote sensing technique for global monitoring of power plant CO$_{2}$ emissions from space and related applications, Atmos. Meas. Tech., 3(4), 781–811, doi:10.5194/amt-3-781-2010, 2010.

Brooker, L.: CONSTELLATION OF SMALL SATELLITES FOR THE MONITORING OF GREENHOUSE GASES, in 69th International Astronautical Congress (IAC)., 2018.

Broquet, G., Bréon, F.-M., Renault, E., Buchwitz, M., Reuter, M., Bovensmann, H., Chevallier, F., Wu, L. and Ciais, P.: The potential of satellite spectro-imagery for monitoring CO$_{2}$ emissions from large cities, Atmos. Meas. Tech., 11(2), 681–708, doi:10.5194/amt-11-681-2018, 2018.

Buchwitz, M., de Beek, R., Burrows, J. P., Bovensmann, H., Warneke, T., Notholt, J., Meirink, J. F., Goede, A. P. H., Bergamaschi, P., Körner, S., Heimann, M. and Schulz, A.: Atmospheric methane and carbon dioxide from SCIAMACHY satellite data: initial comparison with chemistry and transport models, Atmos. Chem. Phys., 5(4), 941–962, doi:10.5194/acp-5-941-2005, 2005.

Buchwitz, M., Reuter, M., Bovensmann, H., Pillai, D., Heymann, J., Schneising, O., Rozanov, V., Krings, T., Burrows, J. P., Boesch, H., Gerbig, C., Meijer, Y. and Löscher, A.: Carbon Monitoring Satellite (CarbonSat): assessment of atmospheric CO$_{2}$ and CH$_{4}$ retrieval errors by error parameterization, Atmos. Meas. Tech., 6(12), 3477–3500, doi:10.5194/amt-6-3477-2013, 2013.

Chedin, A., Scott, N., Wahiche, C. and Moulinier, P.: The Improved Initialization Inversion Method: A High Resolution Physical Method for Temperature Retrievals from Satellites of the TIROS-N Series, J. Clim. Appl. Meteo., 24, 128–143, doi:10.1175/1520-0450(1985)024<0128:TIIIMA>2.0.CO;2, 1985.

Chevallier, F., Chéruy, F., Scott, N. A. and Chédin, A.: A Neural Network Approach for a Fast and Accurate Computation of a Longwave Radiative Budget, J. Appl. Meteorol., 37(11), 1385–1397, doi:https://doi.org/10.1175/1520-0450(1998)037<1385:ANNAFA>2.0.CO;2, 1998.

Chevallier, F., Bréon, F.-M. and Rayner, P. J.: Contribution of the Orbiting Carbon Observatory to the estimation of CO2 sources and sinks: Theoretical study in a variational data assimilation framework, J. Geophys. Res. Atmos., 112(D9), doi:10.1029/2006JD007375, 2007.

Chevallier, F., Remaud, M., O'Dell, C. W., Baker, D., Peylin, P. and Cozic, A.: Objective evaluation of surface- and satellite-driven carbon dioxide atmospheric inversions, Atmos. Chem. Phys., 19(22), 14233–14251, doi:10.5194/acp-19-14233-2019, 2019.

Ciais, P., Rayner, P., Chevallier, F., Bousquet, P., Logan, M., Peylin, P. and Ramonet, M.: Atmospheric inversions for estimating CO2 fluxes: methods and perspectives, Clim. Change, 103(1), 69–92, doi:10.1007/s10584-010-9909-3, 2010.

Connor, B. J., Boesch, H., Toon, G., Sen, B., Miller, C. and Crisp, D.: Orbiting Carbon Observatory: Inverse method and prospective error analysis, J. Geophys. Res. Atmos., 113(D5), doi:10.1029/2006JD008336, 2008.

Crisp, D., Pollock, H. R., Rosenberg, R., Chapsky, L., Lee, R. A. M., Oyafuso, F. A., Frankenberg, C., O'Dell, C. W., Bruegge, C. J., Doran, G. B., Eldering, A., Fisher, B. M., Fu, D., Gunson, M. R., Mandrake, L., Osterman, G. B., Schwandner, F. M., Sun, K., Taylor, T. E., Wennberg, P. O. and Wunch, D.: The on-orbit performance of the Orbiting Carbon Observatory-2 (OCO-2) instrument and its radiometrically calibrated products, Atmos. Meas. Tech., 10(1), 59–81, doi:10.5194/amt-10-59-2017, 2017.

Cusworth, D. H., Duren, R. M., Thorpe, A. K., Eastwood, M. L., Green, R. O., Dennison, P. E., Frankenberg, C., Heckler, J. W., Asner, G. P. and Miller, C. E.: Quantifying Global Power Plant Carbon Dioxide Emissions With Imaging Spectroscopy, AGU Adv., 2(2), e2020AV000350, doi:https://doi.org/10.1029/2020AV000350, 2021.

Dogniaux, M., Crevoisier, C., Armante, R., Capelle, V., Delahaye, T., Cassé, V., De Mazière, M., Deutscher, N. M., Feist, D. G., Garcia, O. E., Griffith, D. W. T., Hase, F., Iraci, L. T., Kivi, R., Morino, I., Notholt, J., Pollard, D. F., Roehl, C. M., Shiomi, K., Strong, K., Té, Y., Velazco, V. A. and Warneke, T.: The Adaptable 4A Inversion (5AI): description and first $X_\chem{CO_2}$ retrievals from Orbiting Carbon Observatory-2 (OCO-2) observations, Atmos. Meas. Tech., 14(6), 4689–4706, doi:10.5194/amt-14-4689-2021, 2021.

Dogniaux, M., Crevoisier, C., Gousset, S., Le Coarer, É., Ferrec, Y., Croizé, L., Wu, L., Hasekamp, O., Sic, B. and Brooker, L.: The Space Carbon Observatory (SCARBO) concept: assessment of $X_{\mathrm{CO}_{2}}$ and $X_{\mathrm{CH}_{4}}$ retrieval performance, Atmos. Meas. Tech., 15(16), 4835–4858, doi:10.5194/amt-15-4835-2022, 2022.

Duren, R. M. and Miller, C. E.: Measuring the carbon emissions of megacities, Nat. Clim. Chang., 2(8), 560–562, doi:10.1038/nclimate1629, 2012.

Friedlingstein, P., O'Sullivan, M., Jones, M. W., Andrew, R. M., Gregor, L., Hauck, J., Le Quéré, C., Luijkx, I. T., Olsen, A., Peters, G. P., Peters, W., Pongratz, J., Schwingshackl, C., Sitch, S., Canadell, J. G., Ciais, P., Jackson, R. B., Alin, S. R., Alkama, R., Arneth, A., Arora, V. K., Bates, N. R., Becker, M., Bellouin, N., Bittig, H. C., Bopp, L., Chevallier, F., Chini, L. P., Cronin, M., Evans, W., Falk, S., Feely, R. A., Gasser, T., Gehlen, M., Gkritzalis, T., Gloege, L., Grassi, G., Gruber, N., Gürses, Ö., Harris, I., Hefner, M., Houghton, R. A., Hurtt, G. C., Iida, Y., Ilyina, T., Jain, A. K., Jersild, A., Kadono, K., Kato, E., Kennedy, D., Klein Goldewijk, K., Knauer, J., Korsbakken, J. I., Landschützer, P., Lefèvre, N., Lindsay, K., Liu, J., Liu, Z., Marland, G., Mayot, N., McGrath, M. J., Metzl, N., Monacci, N. M., Munro, D. R., Nakaoka, S.-I., Niwa, Y., O'Brien, K., Ono, T., Palmer, P. I., Pan, N., Pierrot, D., Pocock, K., Poulter, B., Resplandy, L., Robertson, E., Rödenbeck, C., Rodriguez, C., Rosan, T. M., Schwinger, J., Séférian, R., Shutler, J. D., Skjelvan, I., Steinhoff, T., Sun, Q., Sutton, A. J., Sweeney, C., Takao, S., Tanhua, T., Tans, P. P., Tian, X., Tian, H., Tilbrook, B., Tsujino, H., Tubiello, F., van der Werf, G. R., Walker, A. P., Wanninkhof, R., Whitehead, C., Willstrand Wranne, A., et al.: Global Carbon Budget 2022, Earth Syst. Sci. Data, 14(11), 4811–4900, doi:10.5194/essd-14-4811-2022, 2022.

Galli, A., Guerlet, S., Butz, A., Aben, I., Suto, H., Kuze, A., Deutscher, N. M., Notholt, J., Wunch, D., Wennberg, P. O., Griffith, D. W. T., Hasekamp, O. and Landgraf, J.: The impact of spectral resolution on satellite retrieval accuracy of CO$_{2}$ and CH$_{4}$, Atmos. Meas. Tech., 7(4), 1105–1119, doi:10.5194/amt-7-1105-2014, 2014.

Gousset, S., Croizé, L., Le Coarer, E., Ferrec, Y., Rodrigo-Rodrigo, J., Brooker, L. and consortium, for the S.: NanoCarb hyperspectral sensor: on performance optimization and analysis for greenhouse gas monitoring from a constellation of small satellites, CEAS Sp. J., 11(4), 507–524, doi:10.1007/s12567-019-00273-9, 2019.

Hamlin, L., Green, R. O., Mouroulis, P., Eastwood, M., Wilson, D., Dudik, M. and Paine, C.: Imaging spectrometer science measurements for Terrestrial Ecology: AVIRIS and new developments, in 2011 Aerospace Conference, pp. 1–7., 2011.

Hess, M., Koepke, P. and Schult, I.: Optical Properties of Aerosols and Clouds: The Software Package OPAC, Bull. Am. Meteorol. Soc., 79(5), 831–844, doi:https://doi.org/10.1175/1520-0477(1998)079<0831:OPOAAC>2.0.CO;2, 1998.

Houweling, S., Hartmann, W., Aben, I., Schrijver, H., Skidmore, J., Roelofs, G.-J. and Breon, F.-M.: Evidence of systematic errors in SCIAMACHY-observed CO$_{2}$ due to aerosols, Atmos. Chem. Phys., 5(11), 3003–3013, doi:10.5194/acp-5-3003-2005, 2005.

Inoue, M., Morino, I., Uchino, O., Nakatsuru, T., Yoshida, Y., Yokota, T., Wunch, D., Wennberg, P. O., Roehl, C. M., Griffith, D. W. T., Velazco, V. A., Deutscher, N. M., Warneke, T., Notholt, J., Robinson, J., Sherlock, V., Hase, F., Blumenstock, T., Rettinger, M., Sussmann, R., Kyrö, E., Kivi, R., Shiomi, K., Kawakami, S., De Mazière, M., Arnold, S. G., Feist, D. G., Barrow, E. A., Barney, J., Dubey, M., Schneider, M., Iraci, L. T., Podolske, J. R., Hillyard, P. W., Machida, T., Sawa, Y., Tsuboi, K., Matsueda, H., Sweeney, C., Tans, P. P., Andrews, A. E., Biraud, S. C., Fukuyama, Y., Pittman, J. V, Kort, E. A. and Tanaka, T.: Bias corrections of GOSAT SWIR XCO$_{2}$ and XCH$_{4}$ with TCCON data and their evaluation using aircraft measurement data, Atmos. Meas. Tech., 9(8), 3491–3512, doi:10.5194/amt-9-3491-2016, 2016.

IPCC: Summary for Policymakers, edited by V. Masson-Delmotte, P. Zhai, A. Pirani, S. L. Connors, C. Péan, S. Berger, N. Caud, Y. Chen, L. Goldfarb, M. I. Gomis, M. Huang, K. Leitzell, E. Lonnoy, J. B. R. Matthews, T. K. Maycock, T. Waterfield, O. Yelekçi, R. Yu, and B. Zhou, Cambridge University Press, Cambridge, UK and New York, NY, USA., 2021.

Jacquinet-Husson, N., Armante, R., Scott, N. A., Chédin, A., Crépeau, L., Boutammine, C., Bouhdaoui, A., Crevoisier, C., Capelle, V., Boonne, C., Poulet-Crovisier, N., Barbe, A., Benner], D. [Chris, Boudon, V., Brown, L. R., Buldyreva, J., Campargue, A., Coudert, L. H., Devi, V. M., Down, M. J., Drouin, B. J., Fayt, A., Fittschen, C., Flaud, J.-M., Gamache, R. R., Harrison, J. J., Hill, C., Hodnebrog, Ø., Hu, S.-M., Jacquemart, D., Jolly, A., Jiménez, E., Lavrentieva, N. N., Liu, A.-W., Lodi, L., Lyulin, O. M., Massie, S. T., Mikhailenko, S., Müller, H. S. P., Naumenko, O. V, Nikitin, A., Nielsen, C. J., Orphal, J., Perevalov, V. I., Perrin, A., Polovtseva, E., Predoi-Cross, A., Rotger, M., Ruth, A. A., Yu, S. S., Sung, K., Tashkun, S. A., Tennyson, J., Tyuterev, V. G., Auwera], J. [Vander, Voronin, B. A. and Makie, A.: The 2015 edition of the GEISA spectroscopic database, J. Mol. Spectrosc., 327, 31–72, doi:https://doi.org/10.1016/j.jms.2016.06.007, 2016.

Janssens-Maenhout, G., Pinty, B., Dowell, M., Zunker, H., Andersson, E., Balsamo, G., Bézy, J.-L., Brunhes, T., Bösch, H., Bojkov, B., Brunner, D., Buchwitz, M., Crisp, D., Ciais, P., Counet, P., Dee, D., van der Gon, H. D., Dolman, H., Drinkwater, M. R., Dubovik, O., Engelen, R., Fehr, T., Fernandez, V., Heimann, M., Holmlund, K., Houweling, S., Husband, R., Juvyns, O., Kentarchos, A., Landgraf, J., Lang, R., Löscher, A., Marshall, J., Meijer, Y., Nakajima, M., Palmer, P. I., Peylin, P., Rayner, P., Scholze, M., Sierk, B., Tamminen, J. and Veefkind, P.: Toward an Operational Anthropogenic CO2 Emissions Monitoring and Verification Support Capacity, Bull. Am. Meteorol. Soc., 101(8), E1439–E1451, doi:https://doi.org/10.1175/BAMS-D-19-0017.1, 2020.

Krings, T., Gerilowski, K., Buchwitz, M., Reuter, M., Tretner, A., Erzinger, J., Heinze, D., Pflüger, U., Burrows, J. P. and Bovensmann, H.: MAMAP – a new spectrometer system for column-averaged methane and carbon dioxide observations from aircraft: retrieval algorithm and first inversions for point source emission rates, Atmos. Meas. Tech., 4(9), 1735–1758, doi:10.5194/amt-4-1735-2011, 2011.

Kuhlmann, G., Broquet, G., Marshall, J., Clément, V., Löscher, A., Meijer, Y. and Brunner, D.: Detectability of \chem{CO_{2}} emission plumes of cities and power plants with the Copernicus Anthropogenic \chem{CO_{2}} Monitoring (CO2M) mission, Atmos. Meas. Tech., 12(12), 6695–6719, doi:10.5194/amt-12-6695-2019, 2019.

Lamouroux, J., Régalia, L., Thomas, X., Vander Auwera, J., Gamache, R. R. and Hartmann, J.-M.: CO2 line-mixing database and software update and its tests in the 2.1µm and 4.3µm regions, J. Quant. Spectrosc. Radiat. Transf., 151, 88–96, doi:https://doi.org/10.1016/j.jqsrt.2014.09.017, 2015.

Liou, K.-N.: An introduction to atmospheric radiation [electronic resource] / K.N. Liou., 2nd ed., Academic Press, Amsterdam ;, 2002.

Liu, X., Huang, Y., Xu, X., Li, X., Li, X., Ciais, P., Lin, P., Gong, K., Ziegler, A. D., Chen, A., Gong, P., Chen, J., Hu, G., Chen, Y., Wang, S., Wu, Q., Huang, K., Estes, L. and Zeng, Z.: High-spatiotemporal-resolution mapping of global urban change from 1985 to 2015, Nat. Sustain., 3(7), 564–570, doi:10.1038/s41893-020-0521-x, 2020.

Lwasa, S., Seto, K. C., Bai, X., Blanco, H., Gurney, K. R., Kilkiş, S., Lucon, O., Murakami, J., Pan, J., Sharifi, A. and Yamagata, Y.: Urban systems and other settlements, edited by P. R. Shukla, J. Skea, R. Slade, A. Al Khourdajie, R. van Diemen, D. McCollum, M. Pathak, S. Some, P. Vyas, R. Fradera, M. Belkacemi, A. Hasija, G. Lisboa, S. Luz, and J. Malley, Cambridge University Press, Cambridge, UK and New York, NY, USA., 2022.

Matsunaga, T. and Tanimoto, H.: Greenhouse gas observation by TANSO-3 onboard GOSAT-GW, in Sensors, Systems, and Next-Generation Satellites XXVI, vol. 12264, edited by S. R. Babu, A. Hélière, and T. Kimura, p. 122640B, SPIE., 2022.

Meijer, Y.: Copernicus CO$_2$ Monitoring Mission Requierment Document. [online] Available from: https://esamultimedia.esa.int/docs/EarthObservation/CO2M_MRD_v3.0_20201001_Issued.pdf, 2020.

Nassar, R., Mastrogiacomo, J.-P., Bateman-Hemphill, W., McCracken, C., MacDonald, C. G., Hill, T., O'Dell, C. W., Kiel, M. and Crisp, D.: Advances in quantifying power plant CO2 emissions with OCO-2, Remote Sens. Environ., 264, 112579, doi:https://doi.org/10.1016/j.rse.2021.112579, 2021.

Noël, S., Reuter, M., Buchwitz, M., Borchardt, J., Hilker, M., Bovensmann, H., Burrows, J. P., Di Noia, A., Suto, H., Yoshida, Y., Buschmann, M., Deutscher, N. M., Feist, D. G., Griffith, D. W. T., Hase, F., Kivi, R., Morino, I., Notholt, J., Ohyama, H., Petri, C., Podolske, J. R., Pollard, D. F., Sha, M. K., Shiomi, K., Sussmann, R., Té, Y., Velazco, V. A. and Warneke, T.: \chem{XCO_2} retrieval for GOSAT and GOSAT-2 based on the FOCAL algorithm, Atmos. Meas. Tech., 14(5), 3837–3869, doi:10.5194/amt-14-3837-2021, 2021.

O'Dell, C. W., Eldering, A., Wennberg, P. O., Crisp, D., Gunson, M. R., Fisher, B., Frankenberg, C., Kiel, M., Lindqvist, H., Mandrake, L., Merrelli, A., Natraj, V., Nelson, R. R., Osterman, G. B., Payne, V. H., Taylor, T. E., Wunch, D., Drouin, B. J., Oyafuso, F., Chang, A., McDuffie, J., Smyth, M., Baker, D. F., Basu, S., Chevallier, F., Crowell, S. M. R., Feng, L., Palmer, P. I., Dubey, M., Garc\'\ia, O. E., Griffith, D. W. T., Hase, F., Iraci, L. T., Kivi, R., Morino, I., Notholt, J., Ohyama, H., Petri, C., Roehl, C. M., Sha, M. K., Strong, K., Sussmann, R., Te, Y., Uchino, O. and Velazco, V. A.: Improved retrievals of carbon dioxide from Orbiting Carbon Observatory-2 with the version 8 ACOS algorithm, Atmos. Meas. Tech., 11(12), 6539–6576, doi:10.5194/amt-11-6539-2018, 2018.

Pascal, V., Buil, C., Loesel, J., Tauziede, L., Jouglet, D. and Buisson, F.: An improved microcarb dispersive instrumental concept for the measurement of greenhouse gases concentration in the atmosphere, in International Conference on Space Optics — ICSO 2014, vol. 10563, edited by Z. Sodnik, B. Cugny, and N. Karafolas, pp. 1028–1036, SPIE., 2017.

Peiro, H., Crowell, S., Schuh, A., Baker, D. F., O'Dell, C., Jacobson, A. R., Chevallier, F., Liu, J., Eldering, A., Crisp, D., Deng, F., Weir, B., Basu, S., Johnson, M. S., Philip, S. and Baker, I.: Four years of global carbon cycle observed from the Orbiting Carbon Observatory 2 (OCO-2) version 9 and in situ data and comparison to OCO-2 version 7, Atmos. Chem. Phys., 22(2), 1097–1130, doi:10.5194/acp-22-1097-2022, 2022.

Pillai, D., Buchwitz, M., Gerbig, C., Koch, T., Reuter, M., Bovensmann, H., Marshall, J. and Burrows, J. P.: Tracking city CO$_{2}$ emissions from space using a high-resolution inverse modelling approach: a case study for Berlin, Germany, Atmos. Chem. Phys., 16(15), 9591–9610, doi:10.5194/acp-16-9591-2016, 2016.

Rayner, P. J. and O'Brien, D. M.: The utility of remotely sensed CO2 concentration data in surface source inversions, Geophys. Res. Lett., 28(1), 175–178, doi:10.1029/2000GL011912, 2001.

Reuter, M., Buchwitz, M., Schneising, O., Heymann, J., Bovensmann, H. and Burrows, J. P.: A method for improved SCIAMACHY CO$_{2}$ retrieval in the presence of optically thin clouds, Atmos. Meas. Tech., 3(1), 209–232, doi:10.5194/amt-3-209-2010, 2010.

Reuter, M., Buchwitz, M., Schneising, O., Krautwurst, S., O'Dell, C. W., Richter, A., Bovensmann, H. and Burrows, J. P.: Towards monitoring localized \chem{CO_2} emissions from space: co-located regional \chem{CO_2} and \chem{NO_2} enhancements observed by the OCO-2 and S5P satellites, Atmos. Chem. Phys., 19(14), 9371–9383, doi:10.5194/acp-19-9371-2019, 2019.

Roche, S., Strong, K., Wunch, D., Mendonca, J., Sweeney, C., Baier, B., Biraud, S. C., Laughner, J. L., Toon, G. C. and Connor, B. J.: Retrieval of atmospheric CO$_{2}$ vertical profiles from ground-based near-infrared spectra, Atmos. Meas. Tech., 14(4), 3087–3118, doi:10.5194/amt-14-3087-2021, 2021.

Rodgers, C. D.: Inverse Methods for Atmospheric Sounding, WORLD SCIENTIFIC., 2000.

Rusli, S. P., Hasekamp, O., aan de Brugh, J., Fu, G., Meijer, Y. and Landgraf, J.: Anthropogenic CO$_2$ monitoring satellite mission: the need for multi-angle polarimetric observations, Atmos. Meas. Tech., 14(2), 1167–1190, doi:10.5194/amt-14-1167-2021, 2021.

Scott, N. A. and Chédin, A.: A Fast Line-by-Line Method for Atmospheric Absorption Computations: The Automatized Atmospheric Absorption Atlas, J. Appl. Meteorol., 20(7), 802–812, 1981.

Spurr, R. J. D.: Simultaneous derivation of intensities and weighting functions in a general pseudo-spherical discrete ordinate radiative transfer treatment, J. Quant. Spectrosc. Radiat. Transf., 75(2), 129–175, doi:https://doi.org/10.1016/S0022-4073(01)00245-X, 2002.

Strandgren, J., Krutz, D., Wilzewski, J., Paproth, C., Sebastian, I., Gurney, K. R., Liang, J., Roiger, A. and Butz, A.: Towards spaceborne monitoring of localized \chem{CO_2} emissions: an instrument concept and first performance assessment, Atmos. Meas. Tech., 13(6), 2887–2904, doi:10.5194/amt-13-2887-2020, 2020.

Taylor, T. E., O'Dell, C. W., Crisp, D., Kuze, A., Lindqvist, H., Wennberg, P. O., Chatterjee, A., Gunson, M., Eldering, A., Fisher, B., Kiel, M., Nelson, R. R., Merrelli, A., Osterman, G., Chevallier, F., Palmer, P. I., Feng, L., Deutscher, N. M., Dubey, M. K., Feist, D. G., Garc\'\ia, O. E., Griffith, D. W. T., Hase, F., Iraci, L. T., Kivi, R., Liu, C., De Mazière, M., Morino, I., Notholt, J., Oh, Y.-S., Ohyama, H., Pollard, D. F., Rettinger, M., Schneider, M., Roehl, C. M., Sha, M. K., Shiomi, K., Strong, K., Sussmann, R., Té, Y., Velazco, V. A., Vrekoussis, M., Warneke, T. and Wunch, D.: An 11-year record of XCO$_2$ estimates derived from GOSAT measurements using the NASA ACOS version 9 retrieval algorithm, Earth Syst. Sci. Data, 14(1), 325–360, doi:10.5194/essd-14-325-2022, 2022.

Taylor, T. E., O'Dell, C. W., Baker, D., Bruegge, C., Chang, A., Chapsky, L., Chatterjee, A., Cheng, C., Chevallier, F., Crisp, D., Dang, L., Drouin, B., Eldering, A., Feng, L., Fisher, B., Fu, D., Gunson, M., Haemmerle, V., Keller, G. R., Kiel, M., Kuai, L., Kurosu, T., Lambert, A., Laughner, J., Lee, R., Liu, J., Mandrake, L., Marchetti, Y., McGarragh, G., Merrelli, A., Nelson, R. R., Osterman, G., Oyafuso, F., Palmer, P. I., Payne, V. H., Rosenberg, R., Somkuti, P., Spiers, G., To, C., Weir, B., Wennberg, P. O., Yu, S. and Zong, J.: Evaluating the consistency between OCO-2 and OCO-3 XCO$_2$ estimates derived from the NASA ACOS version 10 retrieval algorithm, Atmos. Meas. Tech., 16(12), 3173–3209, doi:10.5194/amt-16-3173-2023, 2023.

Tran, H. and Hartmann, J.-M.: An improved O2 A band absorption model and its consequences for retrievals of photon paths and surface pressures, J. Geophys. Res. Atmos., 113(D18), doi:10.1029/2008JD010011, 2008.

Varon, D. J., Jacob, D. J., McKeever, J., Jervis, D., Durak, B. O. A., Xia, Y. and Huang, Y.: Quantifying methane point sources from fine-scale satellite observations of atmospheric methane plumes, Atmos. Meas. Tech., 11(10), 5673–5686, doi:10.5194/amt-11-5673-2018, 2018.

Wilzewski, J. S., Roiger, A., Strandgren, J., Landgraf, J., Feist, D. G., Velazco, V. A., Deutscher, N. M., Morino, I., Ohyama, H., Té, Y., Kivi, R., Warneke, T., Notholt, J., Dubey, M., Sussmann, R., Rettinger, M., Hase, F., Shiomi, K. and Butz, A.: Spectral sizing of a coarse-spectral-resolution satellite sensor for \chem{XCO_2}, Atmos. Meas. Tech., 13(2), 731–745, doi:10.5194/amt-13-731-2020, 2020.

Wu, L., Hasekamp, O., Hu, H., aan de Brugh, J., Landgraf, J., Butz, A. and Aben, I.: Full-physics carbon dioxide retrievals from the Orbiting Carbon Observatory-2 (OCO-2) satellite by only using the 2.06\,\unit{\mu}m band, Atmos. Meas. Tech., 12(11), 6049–6058, doi:10.5194/amt-12-6049-2019, 2019.

Wu, L., aan de Brugh, J., Meijer, Y., Sierk, B., Hasekamp, O., Butz, A. and Landgraf, J.: \chem{XCO_2} observations using satellite measurements with moderate spectral resolution: investigation using GOSAT and OCO-2 measurements, Atmos. Meas. Tech., 13(2), 713–729, doi:10.5194/amt-13-713-2020, 2020.

Yang, D., Boesch, H., Liu, Y., Somkuti, P., Cai, Z., Chen, X., Di Noia, A., Lin, C., Lu, N., Lyu, D., Parker, R. J., Tian, L., Wang, M., Webb, A., Yao, L., Yin, Z., Zheng, Y., Deutscher, N. M., Griffith, D. W. T., Hase, F., Kivi, R., Morino, I., Notholt, J., Ohyama, H., Pollard, D. F., Shiomi, K., Sussmann, R., Té, Y., Velazco, V. A., Warneke, T. and Wunch, D.: Toward High Precision XCO2 Retrievals From TanSat Observations: Retrieval Improvement and Validation Against TCCON Measurements, J. Geophys. Res. Atmos., 125(22), e2020JD032794, doi:https://doi.org/10.1029/2020JD032794, 2020.

Zheng, B., Chevallier, F., Ciais, P., Broquet, G., Wang, Y., Lian, J. and Zhao, Y.: Observing carbon dioxide emissions over China's cities and industrial areas with the Orbiting Carbon Observatory-2, Atmos. Chem. Phys., 20(14), 8501–8510, doi:10.5194/acp-20-8501-2020, 2020.